Design of a Dual-Axis Capacitive MEMS Accelerometer for Low Cross-Axis Sensitivity and Low Noise using SOIMUMPs Process

Author

Shayaan Saghir

00000274053

Supervisor

Dr. Muhammad Mubasher Saleem

DEPARTMENT OF MECHATRONICS ENGINEERING

COLLEGE OF ELECTRICAL & MECHANICAL ENGINEERING

NATIONAL UNIVERSITY OF SCIENCES AND TECHNOLOGY

ISLAMABAD

APRIL, 2021

Design of a Dual-Axis Capacitive MEMS Accelerometer for Low Cross-Axis Sensitivity and Low Noise using SOIMUMPs Process

Author

SHAYAAN SAGHIR

00000274053

A thesis submitted in partial fulfillment of the requirements for the degree of

MS Mechatronics Engineering

Thesis Supervisor:

DR. MUHAMMAD MUBASHER SALEEM

Thesis Supervisor's Signature: _____

DEPARTMENT OF MECHATRONICS ENGINEERING

COLLEGE OF ELECTRICAL & MECHANICAL ENGINEERING

NATIONAL UNIVERSITY OF SCIENCES AND TECHNOLOGY, ISLAMABAD

APRIL, 2021

Declaration

I certify that this research work titled "*Design of a Dual-Axis Capacitive MEMS Accelerometer for Low Cross-Axis Sensitivity and Low Noise using SOIMUMPs Process"* is my own work. The work has not been presented elsewhere for assessment. I have properly acknowledged / referred the material that has been used from other sources.

Signature of Student

Shayaan Saghir

00000274053

Language Correctness Certificate

This thesis has been read by an English expert and is free of typing, syntax, semantic, grammatical and spelling mistakes. Thesis is also according to the format given by the university.

Signature of Student

Shayaan Saghir

00000274053

Signature of Supervisor

Copyright Statement

- Copyright in text of this thesis rests with the student author. Copies (by any process) either in full, or of extracts, may be made only in accordance with instructions given by the author and lodged in the Library of NUST College of E & ME. Details may be obtained by the Librarian. This page must form part of any such copies made. Further copies (by any process) may not be made without the permission (in writing) of the author.
- The ownership of any intellectual property rights which may be described in this thesis is vested in NUST College of E & ME, subject to any prior agreement to the contrary, and may not be made available for use by third parties without the written permission of the College of E & ME, which will prescribe the terms and conditions of any such agreement.
- Further information on the conditions under which disclosures and exploitation may take place is available from the Library of NUST College of E & ME, Rawalpindi.

Acknowledgements

First and foremost, glory and gratitude to God, Allah Almighty, for showering His blessings on me during my research work, allowing me to successfully complete the research.

I would like to express my heartfelt gratitude to Dr. Muhammad Mubasher Saleem, Ph.D., Asst. Professor and Associate Head of Department of Mechatronics Engineering, my research boss, for allowing me to conduct research and providing invaluable support in the process. His dynamism, vision, honesty, and inspiration have all left an indelible impression on me. He showed me how to do research and how to present research findings as clearly as possible. Working and studying under his direction was a great honour and privilege. I am thankful for everything he has done for me. I would also like to express my gratitude for his friendship, empathy, and good humour. I would like to express my heartfelt gratitude to his wife and family for their acceptance and patience during our talk about research work.

I owe my parents a debt of gratitude for their devotion, prayers, care, and sacrifices in educating and training me for the future. My mother deserves special thanks for her prayers, understanding, and ongoing concern, inspiration, and assistance in helping me finish this research project. I would want to thank my brothers and sister for their unwavering love and prayers. My heartfelt gratitude goes out to my friends and colleagues for their unwavering commitment to seeing this thesis through to completion.

This work is devoted to my adored parents and cherished siblings, who have always encouraged me to do amazing things.

Abstract

This work presents the design of a dual-axis electrostatic MEMS accelerometer to achieve low cross-axis sensitivity and low noise while considering the microfabrication constraints of commercially available multi-user SOIMUMPs process. The suspension beams are designed to minimize the cross-axis coupling and increase mechanical stability. The MEMS accelerometer design is optimized using a new optimization methodology to achieve robust dynamic response in the operating temperature range of $-40\ ^{o}\text{C}$ to $100\ ^{o}\text{C}$. The optimization methodology involves the use of integrated design and analysis of computer experiments, Gaussian process regression, desirability function approach and FEM simulations. The effect of temperature variations on the squeeze film air damping force in the electrostatic sensing combs and corresponding effect on the dynamic response is analyzed and considered in the optimization study. The voltage sensitivity of the proposed MEMS accelerometer design is obtained by the integration of accelerometer behavioral model with the readout electronics in the MATLAB Simulink environment. The input acceleration range for the proposed MEMS accelerometer design is ± 25 g with cross-axis sensitivity less than 0.03 % and total noise equivalent acceleration (TNEA) value of 0.2 $\text{mg}/\sqrt{\text{Hz}}$.

Key Words: *Accelerometer, Computer Experiments, Desirability Function, Finite Element Method (FEM), Gaussian Process Regression (GPR), Latin Hypercube Sampling (LHS), MEMS, Optimization.*

Table of Contents

List of Figures

List of Tables

Acronyms

MEMS	Microelectromechanical Systems
DACE	Design and Analysis of Computer Experiments
GPR	Gaussian Process Regression
LHS	Latin Hypercube Sampling
FEM	Finite Element Method
BNEA	Brownian Noise Equivalent Acceleration
CNEA	Circuit Noise Equivalent Acceleration
TNEA	Total Noise Equivalent Acceleration

Chapter 1: Introduction

1.1 What are MEMS?

The abbreviation MEMS represents microelectromechanical systems, a term first coined around 1987. Alternatively, it is also called microsystems and micromachines in Europe and Japan, respectively. Microelectromechanical systems deal with the miniaturization of mechanical components and systems and their integration with the electronic circuitry. This integration of miniaturized mechanical components such as beams, gears, springs and diaphragms with electrical components to make it as one microsystem and hence to achieve desired functionality at low cost, low power and less size is the basic purpose of MEMS technology. These devices which may vary in size ranging from few micrometers to millimeters are fabricated by exploiting the techniques used for integrated circuit (IC) batch production. The main tasks that can be performed using this technology at microscale include sensing, actuation and control [1].

Form the time when MEMS came into being, a new era of technology started by bringing innovation in biological [2], chemical [3] and physical [4] sensors and actuators and consequently making them smarter time to time. One of the main advantages of the MEMS technology is its compact size it offers for the desired purpose. The characteristic length of any component in a MEMS device is in the range of 0.1 – 1000 μm. Figure 1.1 illustrates the comparison of the size of MEMS devices with the macro world. As Feynman said in his talk “There is plenty of room at the bottom” [5], which meant that there is enough possibility to decrease the size of devices from macro scale to micro scale. Now a days we realize numerous MEMS devices having dimensions within a range of several micrometers to few millimeters. As shown in Fig. 1.1, the size of MEMS devices is much smaller than macro scale devices and are comparable to the things at micro scale. These not only give advantage of using less space but also consume less power and are robust in their functionality.

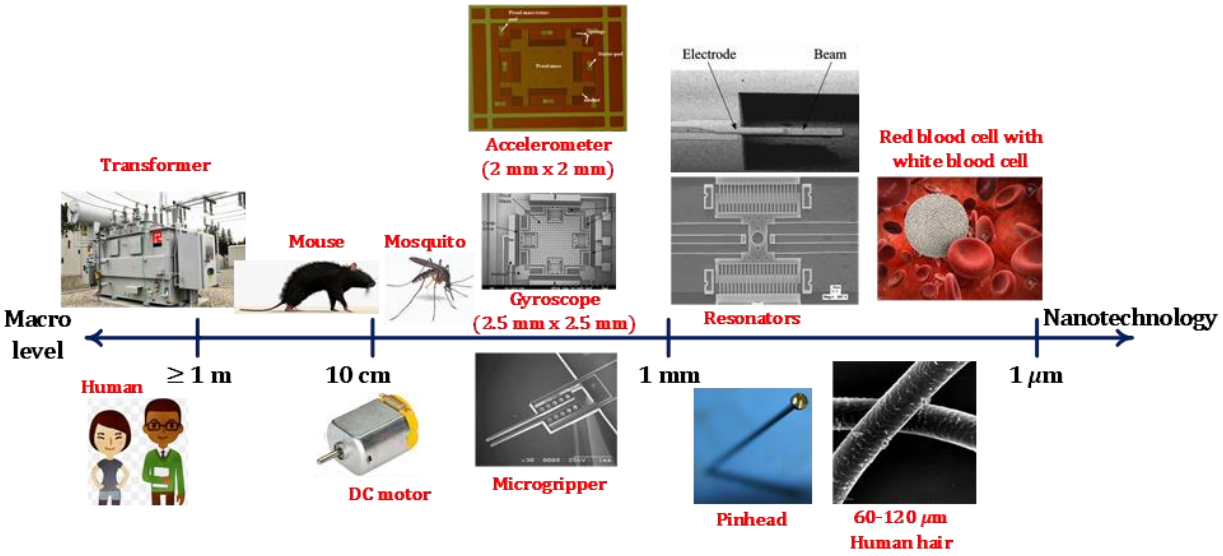

Figure 1.1: Comparison of microscale devices with macro world.

1.2 Benefits of MEMS

Various advantages of using MEMS based technology can be summarized as follows:

- The device can be batch produced in the form of large arrays.
- They are very small in volume and mass and hence take up less space where they are deployed.
- They require less energy and material for their manufacturing.
- They consume very low power for their operation.
- Better sensitivity, accuracy and reliability is achieved.
- Can be easily integrated into systems.
- When produced in large masses, they are very economical.
- Both sensing and actuation can be done simultaneously.

1.3 Applications of MEMS

As the MEMS technology progressed, revealing its more appealing and adjustable features, it resulted in an increased number of its applications in various sectors. A list of various applications of MEMS in different areas is given in Table 1. It can be observed that MEMS has been utilized in almost all the sectors where possible and thus becoming an alternative to macroscale devices. The MEMS devices which have been used intensively include accelerometers,

gyroscopes, magnetometers, microgrippers, pressure sensors, etc. The vast applications of MEMS devices in these areas prove it to be a very promising field.

Table 1: Applications of MEMS in different fields

Sr. No.	Application Area	Usage
1	Biomedical	MEMS actuators as surgical tools, lab on a chip [6] and micro pumps for drug delivery systems [7], proteins and glucose detection in body [8].
2	Consumer electronics	Projection screen, microphones, pressure sensors, inkjet printer heads, data storage, laser scanners, cameras and smart phones [9].
3	Defense	IMUs, Vibration monitoring in aircrafts, energy harvesting based equipment for soldiers, guided systems for ammunition, micro air vehicles, surveillance and embedded sensors [10].
4	Automotive	Temperature and pressure sensors, airbag deployment, tire pressure monitoring, angular and linear position measurement, engine management [11].
5	Industrial	Vibration monitoring in machines, structural health monitoring (S.H.M.), earthquake detection [12].

1.4 MEMS Inertial Sensors

To find out the position of a body in space, a microsystem is required that must have 10 degrees of freedom (DOF) [13]. This can be achieved by designing a system containing a barometer, tri-axial accelerometer, tri-axis gyroscope and a tri-axial magnetometer. All of them are integrated to make as one system which is termed as inertial measurement unit (IMU). MEMS based accelerometers and gyroscopes generally constitute one class of sensors which is called inertial sensors. Micromachined inertial sensors is a very promising class of MEMS based sensors with vast applications in automotive, biomedical and consumer electronics. They are being used in many types of products such as robots, shock monitoring, computer devices, laptops, smart

phones, remotes, cameras, toys, electronic gadgets for gaming and wearable sensors. In medical they are used extensively such as in biomedical devices for monitoring the health of patients. They are also used in vehicles for their maintenance and better operation (active suspension, tire pressure monitoring) and safety of passengers (seat belt and air bag release in case of any jerk).

Evidently, micromachined inertial sensors is a fruitful technology having numerous applications. So, this puts some requirements that these sensors must be available to consumers at lower costs, must work at low power, having small footprint and are robust to environmental changes such temperature and pressure. All these requirements can be carried off using MEMS based inertial sensors which possess above mentioned attributes since they can be batch fabricated into very large volumes at low costs. They offer a very small device size compared to macro scale devices, consume very less power and are robust to imbalances caused by temperature.

Table 2: Performance requirements for various applications of MEMS accelerometers [4]

Application	Dynamic range	Resolution	Bandwidth
Stability in video cameras	$\pm$ 100°/sec	< 0.1°/sec	0-100 Hz
Inertial navigation	$\pm$ 10°/sec	< 10^{-4}°/sec	0-10 Hz
Rollover defense	$\pm$ 100°/sec	< 1°/sec	0-100 Hz
Computer control devices	$\pm$ 100°/sec	< 0.1°/sec	dc-10 Hz
Robots	$\pm$ 10°/sec	< 0.01°/sec	dc-100 Hz

Table 3: Performance requirements for various applications of MEMS gyroscopes [4]

Application	Dynamic range	Resolution	Bandwidth
Inertial navigation	$\pm$ 1 g	< 5 µg	0-100 Hz
Airbag release	$\pm$ 100 g	< 500 mg	0-0.5 kHz
Vibration monitoring	$\pm$ 10 kg	< 100 mg	1-100 kHz
Biomedical	$\pm$ 100 g	< 10 mg	0-100 Hz
Ammunition	$\pm$ 100 kg	1 g	10-100 kHz
Breakable freight shipment	$\pm$ 1 kg	< 100 mg	0-1 kHz
Space/microgravity	$\pm$ 1 g	< 1 µg	0-10 Hz

Tables 2 and 3 lists various applications of MEMS based gyroscopes and accelerometers considering the performance requirements i.e., dynamic range, resolution and bandwidth in each. As it can be seen in the data provided in these tables that a single design of accelerometer or gyroscope cannot be used for all the applications. Generally, a sensor is designed to work for one target application while considering the values of its performance requirements. The values for these requirements are achieved by setting some technical parameters which are also dependent on the dimensions of the mechanical structure.

1.5 MEMS Accelerometers

Microelectromechanical systems (MEMS) based accelerometers have a very high growing demand in the market and played a very vital part in making MEMS a profit-oriented technology [14]. As discussed in previous sections, accelerometers cover various sectors of technology especially automotive and consumer electronics. In their applications, they have become an essential part of the systems such as airbag release, inertial navigation, electronic devices for gaming [15]. Other applications of MEMS accelerometers include structural health monitoring (S.H.M.), seismic or earthquake, control systems for aerospace, wearable devices, patient health monitoring and precision navigation [16]. They are also used to monitor the shipment of easily breakable goods. The use of accelerometers in electronics, smart devices and computers is also increasing day by day as they take up very less space and consume very less power. They are also used in laptops to detect their free fall and hence data in the hard disk can be saved timely before the hit. They are intensively used in vehicles such as for safety purposes to prevent rollover, or in the case of an accident they help to release airbag so that passenger or driver can be protected from severe injury. They are also deployed to maintain the level of headlights and in safety alarm systems. Accelerometers are also extensively used in industry particularly with robots to determine their position and to control their movement. They are installed in machines where vibration monitoring is required to ensure safe operation and better functionality otherwise the machine may experience failure due to prolonged vibrations [17]. Due to these vast number of applications, accelerometers have gained a very high importance and due to this there is plenty of room to pursue research to improve their performance and in parallel reducing the size.

An accelerometer is an electromechanical sensor that is designed to measure different types of acceleration inputs whether static, quasi-static, time varying or dynamic in nature. For any target application, the accelerometer device is designed so that it must be capable of sensing acceleration along all the three orthogonal axes (*x*, *y* and *z*). One approach to do this is by designing a single axis accelerometer and mounting three of them perpendicular to each other along the required axis. In this way each single axis accelerometer would sense input acceleration along its sensitive axis. One advantage of using this topology is that the output signal obtained from any of the axes is not affected from the other two. Though this approach seems to be useful, but this results in larger device dimensions and higher costs for packaging. Moreover, there are chances of misalignment on the design level which occurs due to misalignment of chip package with the die containing structural layer, misalignment of the sensor chip with respect to the PCB board, misalignment between casing and PCB or misalignment of the whole sensor with the surface on which it is installed [18]. A second approach to do this is to integrate three proof masses monolithically on the same substrate where each proof mass is used to sense acceleration along one of the perpendicular axes [19]. A very common issue in this approach is that the all the proof masses have different sensitivities since they have different dimensions and different beams attached to them which result in performance characteristics that are undesirable specially for applications where achieving high performance is the main goal [20]. In addition, the large device size and high sensitivity are still the main limitations in this approach. A third approach to realize multi-axis accelerometers that consist of a single proof mass is that the sensing elements are attached to that single proof mass in such a way that they can sense acceleration along each axis [21]. Unlike previous approaches, this methodology is more likely to output a noisy signal due to the cross-axis sensitivity which can be minimized using additional circuitry and by careful design of beams. However, this technique has several advantages as very small-scale footprint can be achieved and issues such as misalignment and higher packaging costs are avoided. In this scheme, usually a single proof mass is designed and anchored to the substrate with the help of mechanical beams or suspension springs. Under an input acceleration in the sensitive axis, the proof moves along that axis and produces a proportional change in output signal while other axes remain inactive.

1.6 Literature Review

For the categorization of MEMS accelerometers, they can be classified on the basis of either transduction mechanisms or based on output metric and frequency of operation. Broadly, MEMS based accelerometers generally fall into two categories i.e., resonant and non-resonant accelerometers.

Resonant MEMS accelerometers usually require the design of micro-resonators attached to the proof mass and a sensing scheme to transduce the input acceleration to a suitable output signal. Majorly, there are two types of resonant accelerometers that are recently a part of the research. The first type utilizes the shift in frequency of resonators attached to the proof mass. Figure 1.2 shows the design of a single axis resonant MEMS accelerometer reported in literature based on the change in resonant frequency of the resonators attached to the proof mass [22]. As shown in Fig. 1.2(a), the design consists of a proof mass in the center and is anchored to the substrate with the help of fixed guided beams. Two beam resonators are also connected to the proof mass via those mechanical suspension beams. Initially when there is no input acceleration, the two fixed guided beam resonators on either side of the proof mass are oscillating with the same resonant frequency. The driving of resonators is done with the help of driving electrodes attached on one side of the resonator, as shown in Fig. 1.2(b). When an input acceleration is applied in the vertical direction, the proof mass moves along the same direction and thus produces tension and compression in left and right resonators, respectively. This tension and compression cause a decrease and increase in the natural frequency of the resonators. The change in natural frequency of the two resonators is then taken as an output metric. The frequency is measured using the transverse motion of the resonators which is sensed in the form of current through a sensing electrode on the other side of the resonator, as illustrated in Fig. 1.2(b). Several other designs are also presented in literature that use this method of acceleration sensing along with utilizing piezoelectric effect [23], sensitivity controlling mechanisms [24]. These types of accelerometers give quasi-digital output and are usually designed to measure low-g acceleration inputs specially for seismic measurements [25].

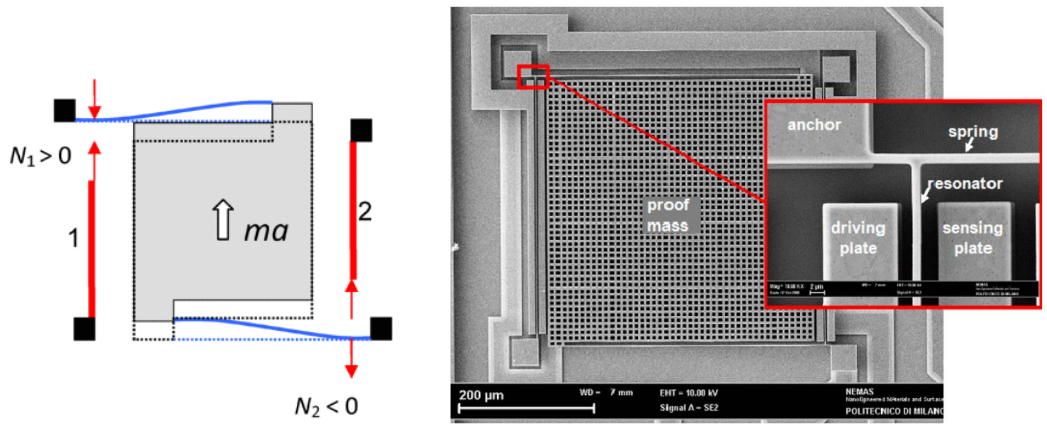

(a) (b)

Figure 1.2: MEMS resonant accelerometer based on frequency shift as output metric [22].

In accelerometer designs that make use of frequency difference as an output metric, the frequency sensitivity is low and is affected due to temperature changes. To enhance the sensitivity, a new methodology is also presented in the literature which amplitude ratio of two resonators is taken as an output metric instead of frequency sensitivity which is considered as second type of MEMS resonant accelerometers. Two similar resonators in a system oscillate at their natural frequency and they are weakly coupled to each other through a mechanical or electrostatic spring of very weak stiffness. Such designs have advantages over previous frequency shift based designs in terms of better common mode rejection ratio (CMRR) capabilities and higher sensitivity [26].

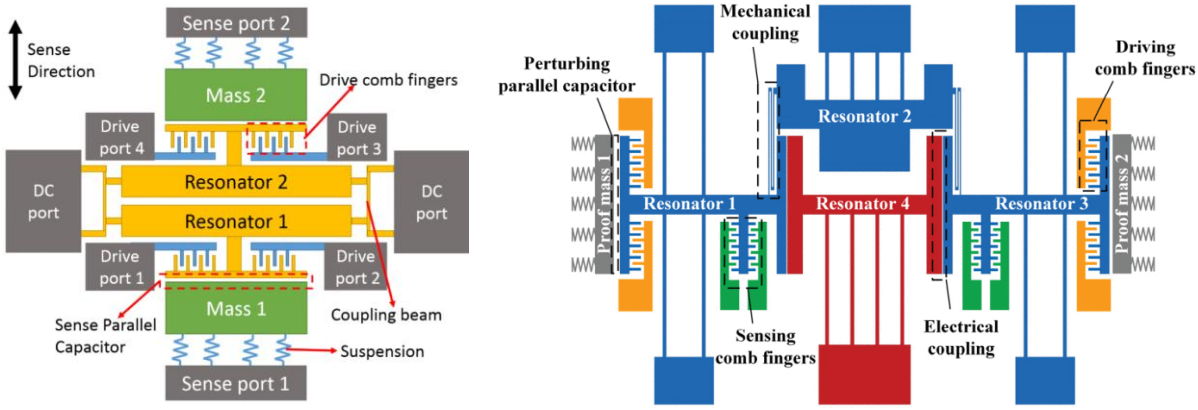

(a) **(b)**

Figure 1.3: Mode localized MEMS resonant accelerometer based on amplitude ratio as output metric [27, 28].

Figure 1.3(a) presents the design of single axis MEMS accelerometer utilizing two resonators weakly coupled to each other [27]. Initially, the resonators are resonating at their natural frequency with equal amplitudes thus giving an amplitude ratio of 1. Due an input acceleration signal, the movement of proof mass changes the electrostatic gap between them and the respective resonators. The closing and closing of the gaps induce positive and negative stiffness perturbation which causes the amplitudes of resonators to changes and thus an amplitude ratio greater than 1 is obtained which is proportional to magnitude of input acceleration. As the research on this methodology progressed, it was found out that integrating a third resonator with two resonator and hence making a 3-DoF system of resonators gives a noticeable increase in amplitude ratio sensitivity. Figure 1.3(b) shows the example of an accelerometer incorporating a system of more than two resonators [28]. An issue in this output metric is that under low values of input acceleration, the amplitude ratio is not a linear function of stiffness perturbation. So, for the same concept, a new modified output is proposed by Pandit et al. [29] in which two resonator systems on each side of the proof mass and instead of considering amplitude ratio, amplitude ratio difference is utilized, thus making the curve linear for the entire range of input acceleration. Likewise frequency shift based resonant accelerometers, these types of accelerometers find their applications in which low-g acceleration sensing is desired. An issue in these resonant MEMS sensors that the resonators suffer from energy dissipation means such as anchor losses due to fluid damping [30].

The second major category of MEMS accelerometer sensors is non-resonant based. These designs usually operate at a frequency lower than natural frequency of the moving structure and their frequency is dependent on the frequency of the input signal. These designs normally consist of a stationary suspended rigid body termed as proof mass. The movement of this proof mass due to an input acceleration gives the measure of the acceleration but this movement has to be transduced using a suitable mechanism. For the design of MEMS based accelerometers specifically which are based on single proof mass, various transduction procedures are adopted in literature. The most common of them include capacitive [31], piezoresistive [32], optical [33], thermal [34] and piezoelectric [35].

All the above-mentioned transduction schemes have their pros and cons as discussed in detail in [17]. The accelerometers that utilize piezoresistive transduction mechanism have

relatively simple structural design, fabrication process and readout electronics but they offer less sensitivity, sensitive to temperature and their device size is large. The capacitive accelerometers have high sensitivity, better dc functioning, little noise and drift and less sensitive to thermal changes yet their performance may alter due to electromagnetic interference. Piezoelectric accelerometers are self-powered, give digital output and have an uncomplicated readout circuitry but due to leakage current in their materials and larger device size, there appears a trade-off in their usage. The advantages of optical accelerometers are that multiple sensors can be multiplexed on

Table 4: Summary of the single proof mass multi-axis capacitive MEMS accelerometers

Reference	Thickness (μm)	Configuration	Size (length×width) μm^2	Input Range (± g)	Sensitivity		Mechanical Cross-axis Sensitivity (%)	BNEA ($\mu g/\sqrt{Hz}$)
					Displacement μm/g	Capacitive (*f*F/g)		
[37]	5	Two axis	1900 μm × 1338 μm (overall)	10	0.029	6.9	-	63
[38]	0.18	Three axis	400 μm × 400 μm (proof mass)	1	5 nm/g	2.46	< 6.6	2100, 2000, 2100
[39]	40	Three axis	450 μm × 450 μm (proof mass)	6	1.72 nm/g	-	3	13, 13, 30
[21]	30	Three axis	1000 μm × 1000 μm (overall)	50	0.01345	10.5, 16.4, 3	1.3, 0.86, 1.05	0.01, 0.1415
[40]	35	Two axis	-	1	0.043	274 mV/g, 280 mV/g	1.26	9.8, 9.9
[41]	6.97	Three axis	515 μm × 425 μm (overall)	-	0.019	11.82, 11.82, 19.93	-	180, 180, 200
[42]	12	Two axis	660 μm × 660 μm (proof mass)	7.5	0.154	0.58	-	0.29
[43]	35	Three axis	11800 μm × 4800 μm (overall)	4	0.036	220	-	13.2
[44]	30	Two axis	2000 μm × 2000 μm (overall)	5	0.02	27	< 2	8.26

the same cable this limiting cost, weight and size and also, they are immune to electromagnetic interference [36].

A conclusion can be drawn from above discussion that MEMS capacitive accelerometers prove to be more suitable for various applications and they are more efficient and reliable. Table 4 presents a summary of single proof mass based MEMS capacitive accelerometer designs presented in the literature. It can be observed that most of the designs have larger thickness for structural layer as required for inertial sensing to overcome mechanical noise. The input acceleration range varies from one design to another because target application is different for each design. To report the sensitivities, three parameters are defined; mechanical or displacement sensitivity (μm/g), capacitance sensitivity (fF/g) and voltage sensitivity (mV/g). As previously discussed, cross-axis sensitivity is a pertaining issue in single proof mass based MEMS accelerometers which need to be minimized. So, cross-axis sensitivities are reported for comparison. For the design of MEMS devices noise considerations are also important to minimize them hence enhancing signal to noise ratio. So, reported mechanical noise for each design is also included in Table 4.

The devices that are inspired from the technology of MEMS involve multiphysics in their working and design. These devices contain more than one performance parameters which need to be optimized for the optimal operation. Different methodologies have been proposed and utilized before to optimize the MEMS devices. The first and simple traditional technique involves the variation of each factor one by one to analyze its dependency on output parameters and thus using the optimized value to make final design while considering geometric and process constraints. This has been done by topology optimization, finite element method (FEM) based models or through mathematical modelling [45-48]. These techniques lose their efficacy when they are used to optimize complex designs involving multiple parameters as they work efficiently with relatively simple designs. Moreover, due to complexity, their computational cost is also on higher side.

For the optimization of MEMS accelerometers several approaches have been proposed. But these approaches again involve optimization of one or two factors using the above-mentioned techniques [49-51]. But for MEMS accelerometers optimizing one or two performance parameters while ignoring others is not a practical approach. Several responses need to be considered while designing for MEMS accelerometers. The responses include natural frequency, displacement

sensitivity, mechanical and electrical noises, pull-in voltage and capacitance sensitivity. Natural frequency depends on the dimensions and stiffness of proof mass. If the natural frequency is kept high, then we can increase the input acceleration to sense, but the displacement sensitivity would be very small. However, if the natural frequency is kept low i.e., low stiffness, then chances of pull-in phenomenon to occur will be increased and input range will be reduced. Similarly, another import aspect is enhancing capacitance output which is a function of parallel plate electrodes overlap length and the gap between them. Smaller the gap would be, larger will be the gap but this leads to high damping between two microstructures and hence mechanical noise will be increased. So, in order to produce an optimal design will considering all above aspects, a suitable and efficient methodology needs to be presented.

The use of statistical techniques to optimize MEMS have been a part of research particularly Design of Experiments (DoE) due to its successful application in various other areas such as pharmacy [52]. farming [53] and several manufacturing operations [54]. In MEMS, the concept of DoE has been utilized extensively to develop response surfaces of RF-MEMS switch [55] and to optimize micromirror [56], RF MEMS switch [57] and MEMS accelerometer [50]. In this traditional methodology, design matrix is explored for the optimization problem of the design through a smaller number of experiments leading us to obtain meta-models for considered optimization parameters. The statistics involved is least-square regression that is due to randomness caused by variations during experiments. This means that DoE demands physical experimentation but due to high cost for fabrication and testing, the use of DoE in MEMS is limited to simulation experiments only which does not output any error. So, the use of statistical model for simulation-based data that is used in case of physical experimentation to get metamodels is ambiguous.

The design and analysis of computer experiments (DACE) is a common technique used by many researchers in various fields to obtain meta-models for output parameters of concern by performing deterministic computer simulations [58-61]. The methodology uses new techniques to make a design matrix for computer experiments such as space filling designs. To develop meta-models, Sack et al. [62] presented a Gaussian process regression (GPR) to be fitted to the data obtained from computer experiments. So, a prospective combination of computer experiments

technique with the simulation tool for MEMS such as FEM can lead to new design optimization methodology and thus can reduce the product development time.

For the capacitive MEMS accelerometers, accurate estimation of the air damping effect on the dynamic response is one of the most important factors that must be considered at the design level. Both slide film and squeeze film air damping mechanisms can drastically change the mechanical sensitivity of the accelerometers [63]. Though, in most of the MEMS accelerometer designs presented in literature, the effect of air damping on the sensor performance has been discussed, but there is lack of detailed investigation of air damping effect on the MEMS accelerometer performance under varying temperature conditions. The effect of air damping on the suspended proof mass of the accelerometers is generally minimized using etch holes or increasing the air gap between the suspended mass and bottom substrate. Thus, choice of microfabrication process technique and its corresponding constraints also play an important role at the design level in minimizing the air damping effect.

In this work, a single mass, dual-axis capacitive MEMS accelerometer design is presented considering the process constraints of commercially available low-cost microfabrication process SOIMUMPs by MEMSCAP Inc [64]. The microfabrication allows to achieve larger structural layer thickness and reduced air damping. The suspension beams are designed to minimize the cross-axis sensitivity and increase the mechanical stability. The design is first optimized while presented a new and efficient optimization technique for MEMS devices. The optimization study is based on design and analysis of computer experiments and involves FEM simulations to optimize several output parameters. A detailed analysis of air damping under varying temperature on the dynamic response of the proposed MEMS accelerometer design is presented. Moreover, both the capacitance and voltage sensitivity values are obtained considering the readout electronics.

Chapter 2: Accelerometer Design and Modelling

In this section, a structural design for a dual-axis capacitive MEMS accelerometer is presented followed by its analytical model and a new optimization methodology to optimize MEMS designs. The analytical model is developed to estimate various output responses such as the displacement of the proof mass and capacitance change. The optimization methodology is developed to optimize various parameters related to the design.

2.1 Structural Design

Figure 2.1 shows the schematic of the proposed MEMS dual-axis accelerometer design developed considering the constraints of SOIMUMPs commercial microfabrication process by MEMSCAP Inc, USA [64]. The central plate is proof mass which is suspended using T-shape suspension beams acting as mechanical springs which are attached to the substrate from the other side. The motivation for using T-shape suspension springs is so that mechanical cross axis sensitivity can be minimized which can affect the performance of dual-axis accelerometers during their operation. To prevent the damage or stiction of the proof mass due to any shock or high acceleration input, circular shaped end stoppers are also attached on each of its four corners. To sense the input acceleration, parallel plate combs are attached on each side of the proof mass. The combs on the top and bottom of the proof mass sense acceleration along *x*-direction while those on the left and right side of the proof mass sense along *y*-direction. The combs on each side of the proof mass are designed to be in the gap and anti-gap configuration so that maximum capacitance change could be obtained [65]. If the combs were kept with same gap widths on either side of the proof mass, then there will be negligible net change in capacitance.

To design the combs with gap anti-gap configuration, a ratio of 3:1 is obtained for anti-gap to gap widths is obtained from literature [66]. However, an optimization technique to find the optimal ratio of gap and anti-gap widths is presented by Mohammed et al. [44] for single and dual-axis accelerometer designs and an optimal ratio of 1:3.45 is obtained. For the proposed design, with the same dimensions of the proof mass, capacitance change is obtained against ratio of 1:3 and 1:3.45 but the obtained difference in the values is very small. The reason is if the gap and anti-

gap ratio of combs is changed from 1:3 to 1:3.45, then it decreases the number of comb pairs since the dimensions of the proof mas are kept the same. Hence, the ratio of 1:3 is used for the proposed design to sense the change in capacitance due to an input acceleration signal. For the widths of smaller and larger gaps, the minimum feature size offered by the fabrication process is checked which is 2 µm between any two parallel surfaces. But keeping in mind the fabrication tolerance, the widths of the smaller and larger gaps are kept as 2.5 µm and 7.5 µm, respectively.

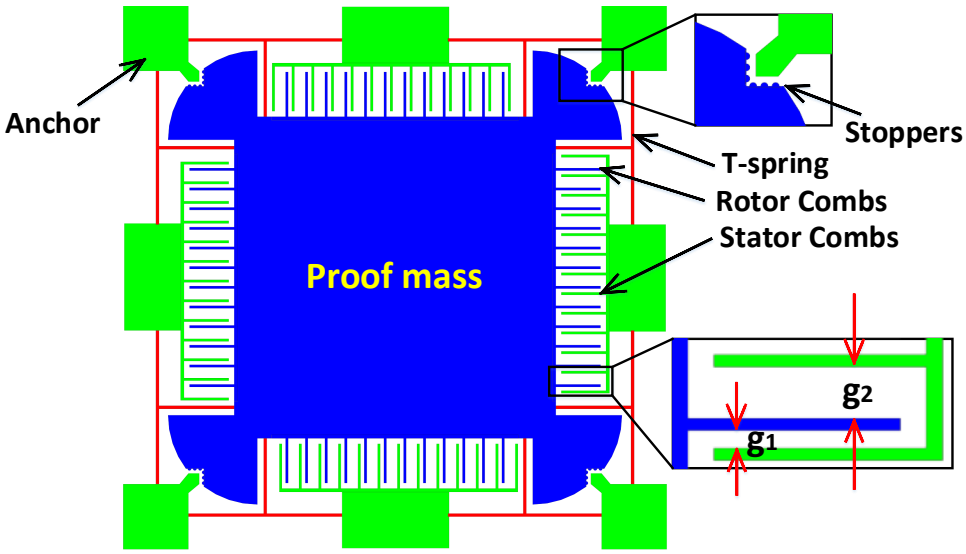

Figure 2.1: 2D schematic of the proposed dual-axis MEMS accelerometer design.

To test the performance of the accelerometer experimentally, it requires acquiring capacitance signal from each set of parallel plate combs to feed into the readout electronics for voltage conversion. To acquire the capacitance signals from the parallel plate combs, needs are placed from on the anchor pads extended after combs. For this purpose, to ensure the better placement of the probe needles, the stators width must be kept larger enough so that they do not damage the combs during their positioning. For the proposed design, the width of the stators is kept 200 µm from each side of the proof mass. The thickness of the whole structure is 25 µm and there is a substantial gap of 400 µm beneath this structural layer. This large gap under the structural layer for the selected microfabrication process is very beneficial as if offers less damping.

2.2 Working Principle and Mathematical Model

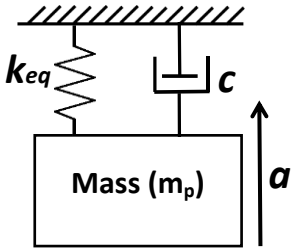

Figure 2.2: Mass-spring-damper model representation for MEMS accelerometer.

The working principle of the accelerometer design can be understood by considering an equivalent mass, spring and damper model. By considering m_p as the value of proof mass, c as the coefficient for air damping and k_{eq} as the overall stiffness of the beams the equation of motion for an input acceleration can be written as [67]:

$$m_p\ddot{x} + c\dot{x} + k_{eq}x = F_0 cos\omega t = m_p a_0 cos\omega t \tag{2.1}$$

where a_0 is the magnitude of the input acceleration at frequency ω and x is the displacement undergone by the proof mass. On solving Eq. (2.1), the following solution for the displacement of the proof mass is obtained:

$$x = \frac{m_p a_0}{\sqrt{\left(k_{eq} - m_p\omega^2\right)^2 + c^2\omega^2}} \tag{2.2}$$

By dividing both the numerator and denominator of Eq. (2.2) with k_{eq} and substituting $\omega_n = \sqrt{\frac{k_{eq}}{m_p}}$ and $\zeta = \frac{c}{2m_p\omega_n}$, we get the following equation:

$$x = \frac{\frac{m_p a_0}{k_{eq}}}{\sqrt{\left\{1 - \left(\frac{\omega}{\omega_n}\right)^2\right\}^2 + \left\{2\zeta\frac{\omega}{\omega_n}\right\}^2}} = \frac{a_0}{\omega_n^2\sqrt{\left\{1 - \left(\frac{\omega}{\omega_n}\right)^2\right\}^2 + \left\{2\zeta\frac{\omega}{\omega_n}\right\}^2}} \tag{2.3}$$

where ω_n is the natural frequency of the mechanical structure and ζ is the damping ratio. Equation (2.3) represents the relationship between applied input acceleration (at any frequency ω) and the resultant displacement in the proof mass given the parameters stiffness, damping and natural

frequency are constant. If the frequency ω in Eq. (2.3) is equal to the natural frequency ω_n, then it takes the following form:

$$\left(\frac{x}{\left(m_p a_0 / k_{eq}\right)}\right)_{\omega=\omega_n} = \frac{1}{2\zeta} = \frac{m_p \omega_n}{c} = Q \tag{2.4}$$

where $\frac{x}{\left(m_p a_0 / k_{eq}\right)}$ is the amplitude ratio and the term Q is the quality factor of the accelerometer proof mass. For MEMS designs working at their resonant frequency, the quality factor is kept as large as possible which is achieved by keeping the natural frequency high and reducing the damping. However, for the devices operating at frequency below natural frequency, the quality factor is kept larger as it also indicates less damping in the system.

2.3 Stiffness of Mechanical Suspension Springs

An issue that occurs in the design of MEMS dual-axis accelerometers is the mechanical cross-axis sensitivity i.e., the undesired movement of the proof mass in the orthogonal direction while measuring movement in the sense direction. So, keeping this aspect in view, T-shaped mechanical suspension springs are designed to suspend the central proof mass. A schematic of the T-spring is shown in Fig. 2.3.

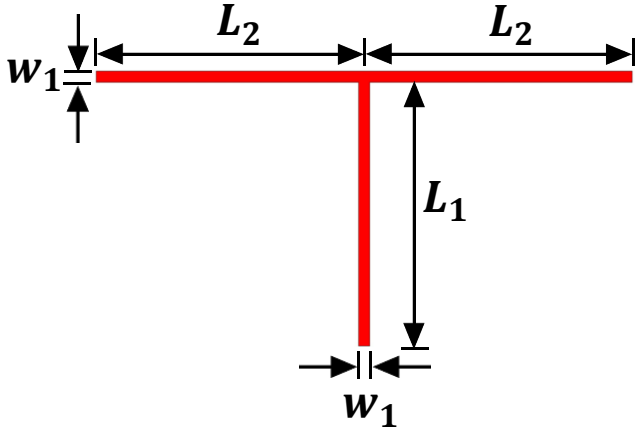

Figure 2.3: Schematic of the T-shaped mechanical suspension spring.

Eight such springs i.e., two for each corner are utilized in which four control the movement along *x*-direction and four along *y*-direction. Assuming that the width of all beams in each spring is equal, the value for the stiffness of one spring can be found analytically as:

$$k_{single} = k_1 + k_2 + k_2 = k_1 + 2k_2 \tag{2.5}$$

where k_1 and k_2 are the stiffnesses for the beams L_1 and L_2, respectively. As discussed above, for an input acceleration along either *x* or *y* axis, four springs control the stiffness. So, the stiffness or overall spring constant can be written as [68]:

$$k_{eq} = 4(k_1 + 2k_2) = 4Et\left(\frac{w_1^3}{L_1^3} + \frac{2w_1^3}{L_2^3}\right) \tag{2.6}$$

where is E the Young's modulus of the material for structural layer and t is the thickness of the structural layer.

2.4 Accelerometer Design Parameters

In this subsection, some design parameters that mostly affect the performance of the accelerometer during its operation are highlighted. The effect of these performance parameters on the output responses are discussed arising the need for their optimization in later sections.

2.4.1 Mechanical Suspension Spring Dimensions

The design of mechanical suspension springs with dimensions for length and width is important as it decides the natural frequency of the system along with the dimensions of the proof mass [69]. Zhang et al. [70] proposed an anti-spring structure to enhance the sensitivity and stability of the proof mass. Similarly, mechanical cross-axis sensitivity is another issue that occurs if the springs are not carefully designed. Hence, spring dimensions are kept based on the targe natural frequency and application.

2.4.2 Sensing Comb Dimensions

For the design of MEMS accelerometers that utilize capacitive transduction, usually parallel plate combs are designed to bring a change in capacitance as result of movement of the

proof mass. Mostly parallel plate capacitance combs are utilized to transduce the displacement of proof mass [44] but efforts have been made to alter the combs shaped such using sloped electrodes with gaps in the nanometers range [71]. One important dimension that is considered is the overlap length between moveable and fixed combs as larger the overlap, larger will be the capacitance output generated, as evident by capacitance formula. Since there is very small gap between two combs, so increasing the overlap length also increases the value for damping coefficient.

2.4.3 Input Acceleration

Since the main task for the design of an accelerometer is to sense the input acceleration. But there is a limit to sense this parameter, the upper limit for which depends on the particular design based on target application. Not all accelerometer designs can sense acceleration in any range. It depends on how the dimensions of the spring elements are set to achieve desired natural frequency. So before working of design, input acceleration range based on the target application is set and hence dimensions of the spring elements and proof mass are set accordingly. This is necessary because if the stiffness of the proof mass is small and hence the natural frequency, then the accelerometer is not capable of measuring high acceleration inputs.

2.4.4 Temperature and Pressure

Another important aspect that needs to be considered in the design of MEMS sensors specially accelerometers is the environmental condition in which the accelerometer is intended to operate. MEMS accelerometers are designed to be operated in various temperature ranges which may start from −40 ℃ to 100 ℃ and as a result of this temperature change, their performance affects resulting in a change in the value of output response such as capacitance change due to the deformation in the structure [72, 73]. Similarly, an accelerometer may be required to operate at room pressure or at vacuum [74]. For a design to operate in the vacuum environment, it is vacuum packaged and hence there is a chance in the deformation of the structure due to the induction of stress [75].

2.5 Accelerometer Performance Parameters

The design of accelerometer requires the achievement of optimal values for the performance parameters. Various parameters need to be considered for the design of MEMS accelerometer to make it suitable to work for the target application. The performance parameters include natural frequency, proof mass displacement, capacitance change, pull-in voltage, Brownian noise equivalent acceleration (BNEA), circuit noise equivalent acceleration (CNEA).

2.5.1 Natural Frequency

The frequency at which the system oscillates with the highest amplitude in the absence of any driving and damping force is known as eigenfrequency or natural frequency of the system. Natural frequency is related to bandwidth and mechanical sensitivity of the accelerometer design and there is a trade-off between them [66]. Lower the natural frequency, higher will be the sensitivity of the design but there is also a decrease in the bandwidth. Natural frequency is given by the following relation:

$$\omega_n = \sqrt{\frac{k_{eq}}{m_p}} \tag{2.7}$$

where k_{eq} is the stiffness of the suspension beams acting as springs, and m_p is the proof mass value. Eq. (2.7) clearly shows that for a specific application, the desired value of natural frequency can be obtained by changing the dimensions of mass and suspension beams.

2.5.2 Proof Mass Displacement

Under an input acceleration, the proof mass of the accelerometer undergoes displacement from its rest position. The amount of this displacement is given by Eq. (2.3) which shows that greater the magnitude of input acceleration, greater will be the magnitude of displacement. However, for a given acceleration magnitude, the amount of displacement that a proof mass undergoes varies due to the change in frequency ω and damping ratio ζ. If the damping in the system is high, then there will be less displacement for the proof mass compared to the displacement in the absence of damping.

2.5.3 Capacitance Change

The accelerometer is designed using a rectangular comb finger type differential capacitive structure as shown in Fig 2.1. With an application of a bias voltage between the proof mass and stator pads, an initial rest capacitance is developed between the sensing gap (g_1) and anti-sensing gap (g_2), as shown in Fig. 3.4 and can be approximated as follows:

$$C_r = \frac{N_c \varepsilon_o l_o t}{g_1} + \frac{N_c \varepsilon_o l_o t}{g_2} \tag{2.8}$$

where C_r is the rest capacitance at static conditions i.e., when no acceleration is applied, N_c is the number of combs on each side of the proof mass, l_o is the overlap length, ε_o is the vacuum permittivity, t is the thickness of combs and g_1 and g_2 are the widths of sensing and anti-sensing gaps, respectively.

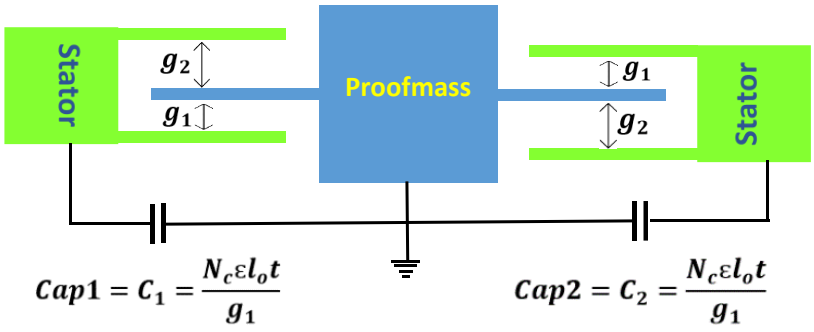

Figure 2.4: Capacitance between proof mass and stator combs.

Since the output metric is the differential capacitance change i.e., difference of the capacitances on both sides of the proof mass. When an input acceleration is experienced the proof mass, the capacitance on one side (say C_1) increases and capacitance on opposite side (C_2) decreases. The change in capacitance ΔC for a displacement x in the proof mass, corresponding to an input acceleration can be calculated for the proposed MEMS accelerometer design as [77]:

$$\Delta C = \frac{2\varepsilon_o t l_o N_c (g_2^2 - g_1^2) x}{(g_1^2 - x^2)(g_2^2 - x^2)} \tag{2.9}$$

The capacitance sensitivity of the MEMS accelerometer can be expressed in terms of scale factor as [78]:

$$S_c = \frac{\Delta C}{a} \text{ (F/g)} \tag{2.10}$$

2.5.4 Pull-in Voltage

To sense the displacement of the proof mass of MEMS accelerometer, corresponding to an input acceleration, initially a bias voltage is applied between the stator and rotor sensing combs. The maximum value of the bias voltage is limited by the pull-in phenomenon. The pull-in occurs for an applied voltage when the electrostatic force overcomes the restoring force of the mechanical spring and moving plate snaps down. The voltage at which this phenomenon occurs is called the pull-in voltage which can be estimated for the MEMS accelerometer as [78]:

$$V_{pi} = \sqrt{\frac{8k_{eq}g_1^3}{27l_o t N_c \varepsilon_0}} \tag{2.11}$$

From Eq. (2.11) it can be seen that the pull-in voltage is a strong function of gap between the combs and the stiffness. The phenomenon of pull-in occurs after the rotor combs have moved one third of their initial distance from stator combs. So, this means to ensure safe operation of the device without any damage, the movement of rotor combs i.e., the proof mass must be below this one third limit for any value of input acceleration.

2.5.5 Brownian Noise Equivalent Acceleration (BNEA)

A phenomenon that occurs with structures with miniaturized dimensions at microscale and placed in environmental conditions of normal pressure is their collision with the molecules of the surrounding medium such as air. This is termed as mechanical-thermal noise and the mechanism is Brownian motion of molecules. The presence of this noise is one of the causes for the performance degradation of MEMS capacitive accelerometers and is called Brownian noise equivalent acceleration (BNEA). The Brownian or thermal-mechanical noise results in a random force acting on the proof mass and is caused primarily due to the damping induced Brownian motion of the air molecules. The value of BNEA can be estimated using the following relation [79]:

$$\text{BNEA} = \sqrt{\frac{4K_B T \omega_n}{m_p Q}} \tag{2.12}$$

where T is the temperature and K_B is the Boltzmann constant. The value of K_B is $1.38 \times 10^{-23} m^2 K g s^{-2} K^{-1}$. Equation (2.12) illustrates that BNEA is dependent on temperature has direct relation with natural frequency and inverse with quality factor indicating that the proof mass with higher resonant frequency will be susceptible to more noise. Similarly, the smaller the damping in the system (i.e., high quality factor), smaller will be the noise.

2.5.6 Circuit Noise Equivalent Acceleration

Another noise that appears during the operation of MEMS accelerometer is the circuit noise equivalent acceleration (CNEA), caused by interface electronics which is used to convert the capacitance change into voltage. CNEA can be calculated as [80]:

$$CNEA = \frac{\Delta C_{min}}{S_c} \tag{2.13}$$

where ΔC_{min} is the resolution of the interface circuit i.e., how small a change in capacitance it can detect and S_c is the scale factor or capacitance sensitivity per unit acceleration. As can be observed from Eq. (2.13) that a larger scale factor is required to overcome this noise and hence to increase signal to noise ratio (SNR).

2.5.7 Total Noise Equivalent Acceleration (TNEA)

The total effect of BNEA and CNEA is calculated by estimating the term called as total noise equivalent acceleration (TNEA) which can be calculated using the relation shown below [69]:

$$TNEA = \sqrt{(BNEA)^2 + (CNEA)^2} \tag{2.14}$$

For the design of MEMS capacitive accelerometer, the objective is to minimize both these noises and hence TNEA.

2.6 Damping in MEMS Capacitive Accelerometer

For the proposed MEMS accelerometer design, both squeeze and slide film damping act as a dissipative mechanism. For an input acceleration in any given axis, the squeeze film damping occurs in the sensing stator and rotor combs in that specific axis while slide film damping occurs in other axis.

2.6.1 Squeeze Film Damping

When a proof mass moves due to an input acceleration, then the combs attached to it moves towards the stator combs thus compressing or squeezing the air between them and as a result the air moves follows the path shown in Fig. 2.5.

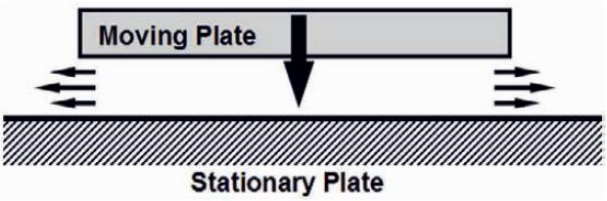

Figure 2.5: Movement of fluid due to squeezing effect between two parallel plates.

For the proposed design, the squeeze film damping is more dominant and is dependent on the viscous, elastic and inertial effects of the air film present between the stator and rotor combs. The kinetic state of the thin air film can be divided into different flow regimes based on the Knudsen number K_n as shown in Table. 5.

Table 5: Classification of flow regimes based on Knudsen number [81]

Flow Regime	Range
Viscous flow	$K_n < 0.01$
Slip flow	$0.01 < K_n < 0.1$
Intermediate flow	$0.1 < K_n < 10$
Molecular flow	$K_n > 10$

The term K_n is a dimensionless number and is given as:

$$K_n = \frac{\lambda}{g_1} \tag{2.15}$$

where λ is the mean free path of air at a given operating temperature and pressure and g_1 is the narrowest air gap thickness. The mean free path of the air can be calculated as [82]:

$$\lambda = \frac{\mu}{P}\sqrt{\frac{\pi K_B T}{2m_{air}}} \tag{2.16}$$

Where μ is air viscosity at atmospheric pressure, P is the air pressure, T is the air temperature and K_B is the Boltzman constant. For the MEMS accelerometer design with smallest air gap (g_1) of 2.5 μm, the value of K_n is 0.027 at atmospheric pressure and room temperature. This shows that the flow regime for the proposed MEMS accelerometer design lies within the slip flow at room temperature and pressure. Figure 2.6 shows the variation in the K_n values for temperature variations in the range of −40 ℃ to 100 ℃ with K_n values of 0.0236 and 0.0299 at −40 ℃ and 100 ℃, respectively. This shows that for the MEMS accelerometer design, the slip flow regime remains valid in the desired temperature range of −40 ℃ to 100 ℃.

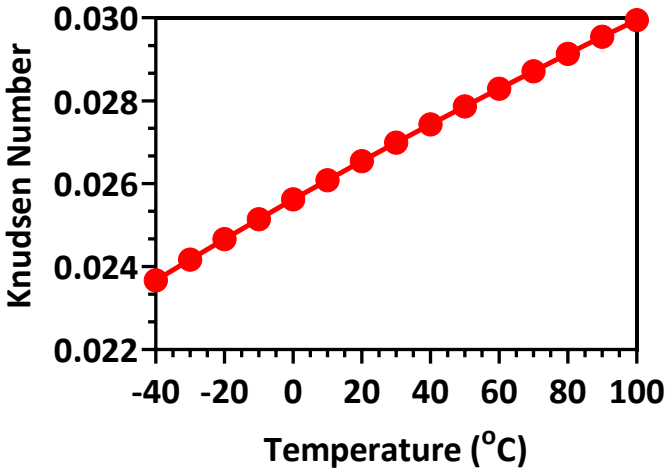

Figure 2.6: Effect of change in temperature on Knudsen number.

The damping force, acting on proof mass in the MEMS accelerometer, is composed of viscous and elastic force components. The relative contribution of these two forces is generally evaluated using a dimensionless squeeze number σ which is given as:

$$\sigma = \frac{12\mu_{eff} t^2 \omega}{P g_1^2} \tag{2.17}$$

where t is the characteristic length and represents the thickness of the stator and rotor combs, μ_{eff} is the effective viscosity, P is the air pressure and g_1 is the sensing gap size and ω is the radial frequency. At low σ values (which is dependent on the frequency of vibrations of proof mass and μ_{eff} value at atmospheric pressure), the thin air film between the stator and rotor combs is not compressed completely and viscous damping force dominates. However, at high σ values (due to high values of ω or μ_{eff}), the thin film air film between the stator and rotor combs fails to escape and elastic force component dominates. The term μ_{eff} is the air viscosity in the slip flow regime and its value is lower than the actual air viscosity. The μ_{eff} is dependent on the K_n value and can be approximated as [83]:

$$\mu_{eff} = \frac{\mu}{1 + 9.638 K_n^{1.1}} \tag{2.18}$$

Considering Eq. (2.18), it can be deduced that the squeeze number value and hence whether dominant damping force mechanism will be viscous, or elastic is dependent on the MEMS accelerometer operating temperature. Figure 2.7 shows the effect of temperature variations in the range of −40 ℃ to 100 ℃ on the squeeze number.

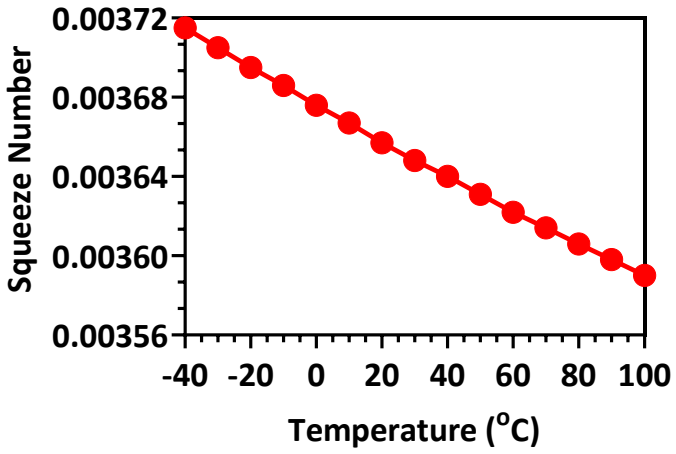

Figure 2.7: Squeeze number vs. temperature graph for a range of −40 ℃ to 100 ℃.

In addition to the thin film air rarefaction and compressibility, the inertia of the air can also contribute towards the damping force in the MEMS accelerometer. The thin film air has the maximum effect of inertia at the widest channel of flow i.e., along the length of combs in accelerometer. This inertial effect can be explained by estimating the Reynolds number which is given as [84]:

$$R_e = \frac{g_1^2 \rho \omega}{\mu_{eff}} \tag{2.19}$$

where g_1 is the width of sensing gap, ρ is the density of air and ω is the operating frequency of the MEMS accelerometer. For low values of Reynolds number i.e., R_e <<1, the inertial effects are very small and hence can be ignored. Figure 2.8 shows the effect of the temperature variations in the range of −40 ℃ to 100 ℃ on the Reynolds number for a fixed value of g_1, ω and ρ. The results show that since the R_e << 1 in this temperature range, the inertial damping effects can be ignored.

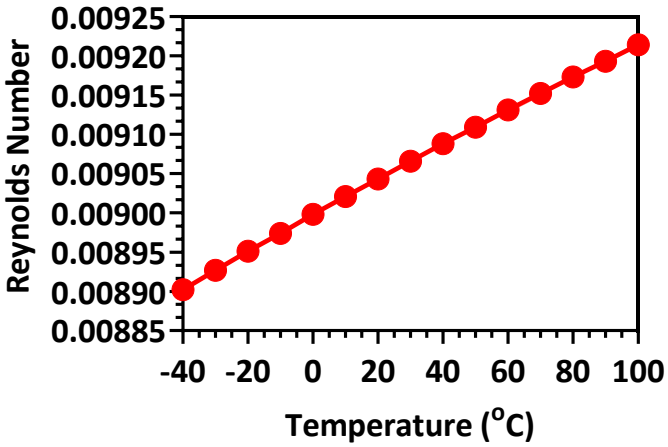

Figure 2.8: Change in Reynolds number due to the shift in temperature from −40 ℃ to 100 ℃.

For the proposed MEMS accelerometer design, the squeeze film air damping coefficient can be calculated as:

$$b_{sq1} = N_c \mu_{eff}\, l_o \left(\frac{t}{g_1}\right)^3 \tag{2.20}$$

$$b_{sq2} = N_c \mu_{eff}\, l_o \left(\frac{t}{g_2}\right)^3 \tag{2.21}$$

where N_c is the number comb fingers along each edge of the proof mass, l_o is the overlap length, μ_{eff} is the effective viscosity of the air and t is the thickness of the combs. The overall squeeze film damping coefficient b_{sq} is thus given as:

$$b_{sq} = b_{sq1} + b_{sq2} \tag{2.22}$$

2.6.2 Slide Film Damping

For structures having miniaturized dimensions at micro scale and moving parallel to a surface, they tend to slide the air film between them. This phenomenon is referred to as slide film damping and the path followed by the fluid is illustrated by Fig. 2.9.

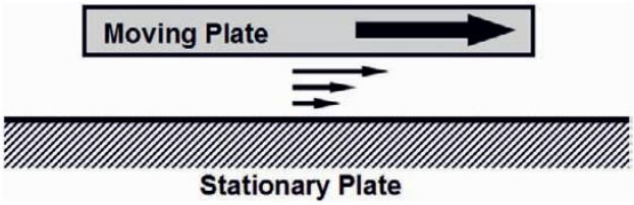

Figure 2.9: Slide film damping between two parallel plate microstructures.

In addition to the squeeze film air damping, the slide film air damping also affects the dynamic response of the MEMS accelerometer when the rotor combs move parallel to the stator combs. The slide film damping coefficient for the MEMS accelerometer can be estimated as:

$$b_{sl1} = \frac{N_c \mu_{eff} A}{g_1} \tag{2.23}$$

$$b_{sl2} = \frac{N_c \mu_{eff} A}{g_2} \tag{2.24}$$

where b_{sl1} and b_{sl2} are slide film damping coefficients due to smaller and larger air gaps respectively, N_c is the number of combs on each side of the proof mass, A is the overlap area of the combs and g_1 and g_2 are widths of sensing and anti-sensing gaps respectively. The overall slide film coefficient b_{sl} is the sum of b_{sl1} and b_{sl2}.

The squeeze and slide film air damping values for the MEMS accelerometer are calculated to be $5.98 \times 10^{-4}\ Ns/m$ and $3.84 \times 10^{-6}\ Ns/m$ respectively. This shows that for the proposed

MEMS accelerometer design, the main damping mechanism is squeeze film air damping. The damping ratio ζ containing the effect of both b_{sq} and b_{sl} can be calculated as [85]

$$\zeta = \frac{c}{2m_p\omega_n} = \frac{b_{sq} + b_{sl}}{2m_p\omega_n} \tag{2.25}$$

where m_p is the value of proof mass, ω_n is the natural frequency and c is overall damping coefficient containing the effect of both squeeze and slide film damping.

Chapter 3: Design and Analysis of Computer Experiments (DACE) based Optimization of MEMS Accelerometer

The methodology adopted to optimize a proposed MEMS dual-axis accelerometer design is discussed in this section. The optimization process is based on computer simulation experiments and for this purpose, a design space containing various combinations of input factors is created. To develop the regression meta-models for each output parameter, Gaussian Process Regression (GPR) model is used, an overview of which is presented in this section. The optimized values for input factors are obtained using desirability function approach and verified through simulations.

3.1 Gaussian Process Regression (GPR)

The problems regarding machine learning are generally categorized into three classes i.e., reinforcement learning, supervised learning and unsupervised learning. Out of these three, supervised learning is mostly taken into account and it is concerned about training a relationship between input and output variables. Considering supervised learning, it may further fall into two categories i.e., regression and classification where outputs are continuous and discrete variables in former and later one, respectively [86].

The models inheriting Gaussian process (GP) in their general form may be used for regression. GP gives the probability distribution over a function i.e., one of the kinds of continuous stochastic processes. When GPs are used is for supervised learning problems such as regression, then it is called Gaussian process regression (GPR) which concerns learning a relationship between outputs and inputs. GP models have been a popular choice to develop regression equations from computer simulation experiments and analyzing the behaviour of deterministic output parameters over the entire design region [87]. In this work, GP model is used to do regression analysis; to find the relationship between output parameters and input factors of the proposed MEMS dual-axis capacitive accelerometer design. A gaussian process model can be represented in the simplest form as [88]:

$$y_i = \mu_z + z(\boldsymbol{x}_i) \tag{3.1}$$

where μ_z is the mean and $z(\boldsymbol{x}_i)$ is the gaussian process containing $\sigma^2\boldsymbol{C}$ term, where σ^2 and $\boldsymbol{C}$ are variance and the matrix for covariance, respectively. For a data set $L_s = (\boldsymbol{x_i}, y_i)$ of R runs, where $i = 1,2, \ldots, R$, y_i represents the value of the output parameter to be optimized and $\boldsymbol{x_i}$ is a L-dimensional input vector of design factor values used in the simulation experiment. The inputs and outputs in k runs can be represented in matrix form i.e., $\boldsymbol{X} = [\boldsymbol{x_1}, \boldsymbol{x_2}, \ldots, \boldsymbol{x_R}]$ and $\boldsymbol{y} = [\boldsymbol{y_1}, \boldsymbol{y_2}, \ldots, \boldsymbol{y_R}]$ respectively. To find the relationship of output parameter with inputs, an arbitrary regression function $z(\boldsymbol{x})$ is determined and it is assumed that the $\boldsymbol{z} = [z(\boldsymbol{x_1}), z(\boldsymbol{x_2}), \ldots, z(\boldsymbol{x_R})]^{\boldsymbol{T}}$ acts according to relative to Gaussian process, with mean zero and covariance $\sigma^2\boldsymbol{C}$, which can be written as [89]:

$$p(\boldsymbol{z}|\boldsymbol{X}) = N(0, \sigma^2\boldsymbol{C}) \tag{3.2}$$

where $\boldsymbol{C}$ represents the covariance matrix that encodes the prior of our understanding between functions $z(\boldsymbol{x_i})$ and $z(\boldsymbol{x_j})$. The matrix $\boldsymbol{C}$ has elements $C_{ij} = c(\boldsymbol{x_i}, \boldsymbol{x_j})$ and can be represented in matrix form as [90]:

$$C(\boldsymbol{X}, \boldsymbol{X}) = \begin{bmatrix} c(\boldsymbol{x}_1, \boldsymbol{x}_1) & c(\boldsymbol{x}_1, \boldsymbol{x}_2) & \cdots & c(\boldsymbol{x}_1, \boldsymbol{x}_R) \\ c(\boldsymbol{x}_1, \boldsymbol{x}_1) & c(\boldsymbol{x}_1, \boldsymbol{x}_2) & \cdots & c(\boldsymbol{x}_2, \boldsymbol{x}_R) \\ \vdots & \vdots & \vdots & \vdots \\ c(\boldsymbol{x}_k, \boldsymbol{x}_1) & c(\boldsymbol{x}_k, \boldsymbol{x}_2) & \cdots & c(\boldsymbol{x}_R, \boldsymbol{x}_R) \end{bmatrix} \tag{3.3}$$

To estimate the entries of the above matrix, a suitable covariance function is needed, the selection for which is very crucial to be used for Gaussian process regression (GPR). The first restriction for using covariance function is that it should give out a nonnegative and definite matrix given by Eq. (3.3). Similarly, from GP prior, some properties are revealed like smoothness, amplitude and length scale. A variety of covariance functions are available (e.g., Matérn, polynomial, squared exponential, rational quadratic and neural network) and any one of them can be selected given such that the matrix retains itself to be positive semi-definite and symmetric. For our case, the most used squared exponential is selected, given as:

$$c(\boldsymbol{x}_a, \boldsymbol{x}_b) = exp\left(-\sum_{i=1}^{L} \theta_i (\boldsymbol{x}_{at} - \boldsymbol{x}_{bt})^2\right) \tag{3.4}$$

where L is the number of factors (dimensions of input matrix), $\boldsymbol{x}_{at}$ and $\boldsymbol{x}_{bt}$ are the values of i^{th} factor for subjects a and b respectively. The term θ_i ($\theta_i \geq 0$) is the hyperparameter and $\theta_i = 0$ means that covariance equals to 1 across the range for that i^{th} factor and the surface fit by used model is planar across that specific region.

After training the data set, the task for fitting GPR is to estimate the arrangement of the estimations of function $\boldsymbol{z}^t$ at test inputs $\boldsymbol{X}^t = [\boldsymbol{x}_1^t, \boldsymbol{x}_2^t, \dots, \boldsymbol{x}_p^t]$. To do this, it is assumed that the isotropic Gaussian is used to distribute output parameter $\boldsymbol{y}$ over $\boldsymbol{z}$ and input $\boldsymbol{X}$ i.e.,

$$p(\boldsymbol{y}|\boldsymbol{z}, \boldsymbol{X}) = N(0, \sigma_R^2 \boldsymbol{I}) \tag{3.5}$$

In Eq. (3.5), $\boldsymbol{I}$ represents $k \times 1$ identity matrix. Using the marginalization property for Gaussian, we can get the marginal distribution for $\boldsymbol{y}$ against input factors $\boldsymbol{X}$ which is given by equation as follows:

$$p(\boldsymbol{y}|\boldsymbol{X}) = p(\boldsymbol{y}|\boldsymbol{z}, \boldsymbol{X})\, p(\boldsymbol{z}|\boldsymbol{X})\, d\boldsymbol{z} = N(0, \boldsymbol{C} + \sigma_R^2 \boldsymbol{I}) \tag{3.6}$$

After the selection of mean and prior covariance functions, we can evaluate posterior by first finding the joint distribution of the trained values of output parameters and those values at test points and then the predictive distribution by implementing the fundamental steps for conditioning Gaussian as:

$$\begin{bmatrix} \boldsymbol{y} \\ \boldsymbol{z}^t \end{bmatrix} \sim N\left(0, \begin{bmatrix} \boldsymbol{C}(\boldsymbol{X}, \boldsymbol{X}) + \sigma^2 \boldsymbol{I} & \boldsymbol{C}(\boldsymbol{X}, \boldsymbol{X}^t) \\ \boldsymbol{C}(\boldsymbol{X}^t, \boldsymbol{X}) & \boldsymbol{C}(\boldsymbol{X}^t, \boldsymbol{X}^t) \end{bmatrix}\right) \tag{3.7}$$

$$p(\boldsymbol{z}^t|\boldsymbol{X}^t, \boldsymbol{y}, \boldsymbol{X}) \sim N(\widehat{\boldsymbol{z}^t}, cv(\boldsymbol{z}^t)) \tag{3.8}$$

$$\widehat{\boldsymbol{z}^t} = \boldsymbol{C}(\boldsymbol{X}^t, \boldsymbol{X})[\boldsymbol{C}(\boldsymbol{X}, \boldsymbol{X}) + \sigma^2 \boldsymbol{I}]^{-1} \boldsymbol{y} \tag{3.9}$$

$$\begin{aligned} v(\boldsymbol{z}^t) = {} & \boldsymbol{C}(\boldsymbol{X}^t, \boldsymbol{X}^t) - \boldsymbol{C}(\boldsymbol{X}^t, \boldsymbol{X})[\boldsymbol{C}(\boldsymbol{X}, \boldsymbol{X}) + \sigma^2 \boldsymbol{I}]^{-1} \boldsymbol{C}(\boldsymbol{X}, \boldsymbol{X}^t) \\ = {} & 1 - \boldsymbol{C}(\boldsymbol{X}^t, \boldsymbol{X})[\boldsymbol{C}(\boldsymbol{X}, \boldsymbol{X}) + \sigma^2 \boldsymbol{I}]^{-1} \boldsymbol{C}(\boldsymbol{X}, \boldsymbol{X}^t) \end{aligned} \tag{3.10}$$

where $\widehat{\boldsymbol{z}^t}$ and $cv(\boldsymbol{z}^t)$ represents mean and covariance of the output estimates of function values at test points. Here the test points will be the optimal values that we would obtain from desirability function approach in later section. The value of hyperparameter θ in Eqs. (3.9) and (3.10) is fit by minimizing the negative log marginal likelihood as given by following equation [86]:

$$-log\, p(\boldsymbol{y}|\boldsymbol{X},\theta) = \frac{1}{2} log|\boldsymbol{C} + \sigma_k^2 \boldsymbol{I}| + \frac{1}{2}\boldsymbol{y}^T(\boldsymbol{C} + \sigma_k^2 \boldsymbol{I})^{-1}\boldsymbol{y} + \frac{k}{2} log 2\pi \quad (3.11)$$

3.2 Input Factors and Output Parameters

For the optimization of MEMS dual-axis accelerometer design, it is important to choose input factors that have greater impact on its operation. The values of output or performance parameters such as natural frequency and proof mass displacement are directly dependent on the dimensions of proof mass and suspension beams [69]. In this study, the dimensions of the proof mass are kept the same because of the limited size of the device. Hence, only the change in dimensions of the suspension beam elements is considered in this optimization study. Since the thickness of the beam (structural layer) is fixed (25 μm), the dimensions that can be varied are the length and width of suspension beam elements such that their optimized values could be obtained. Since the transduction mechanism for the accelerometer operation is capacitive, the factors that affect the capacitance change between combs need to be analyzed. The capacitance between two parallel plates depends on their overlap area and the gap between them (see Eq. (2.8)). The gap between combs is kept fixed, so the only parameter that can be changed is the overlap length and hence its effect on capacitance change and other output parameters is analyzed. The performance of accelerometer in terms of noise is affected due to change in pressure and temperature [71].

Table 6: Input factors for the MEMS dual-axis accelerometer and their corresponding two levels

Code	Input Factors	Lower Value	Upper Value
X_1	Comb Overlap Length (COL)	150 μm	250 μm
X_2	Length of Spring Beam-1 (LSB-1)	400 μm	500 μm
X_3	Length of Spring Beam-2 (LSB-2)	400 μm	500 μm
X_4	Width of Spring Beam (WSB)	6 μm	8 μm
X_5	Input Acceleration (IA)	1 μm	25 μm
X_6	Temperature (T)	233.15 K	373.15 K
X_7	Pressure (P)	100 Torr	760 Torr
X_8	Frequency Ratio (FR)	0.1	0.5

Changing the values of pressure and temperature cause a change in damping coefficients which in turn bring a change in BNEA, thus affecting the performance of the device. So, the effect of temperature and pressure is analyzed while considering them as input factors. The other design factors used in this optimization study are input acceleration and frequency ratio and its impact on proof mass displacement and capacitance change is also analyzed. The input factor frequency ratio is the ratio between obtained natural frequency and any lower frequency in any design run. Table 6 shows the list of the input factors along with their upper and lower values considered in the optimization process.

The first input factor is the comb overlap length, which is varied from 150 μm to 250 μm based on the available space for the device fabrication. The second and third input factors are related to lengths of spring elements, the values for which control their stiffness. The fourth input factor is also related to width of mechanical suspension spring and is also a variable for stiffness function. So, their upper and lower levels are set to change stiffness over a certain range. The fifth one is acceleration input which is considered to analyze its direct relationship with output parameters of interest. The last two input factors are related to surrounding environmental conditions i.e., temperature and pressure. The effect of change in temperature from -40 ℃ to 100 ℃, and pressure from sub-atmospheric (100 Torr) to atmospheric (760 Torr) is also analyzed on output parameters. The last input factor is frequency ratio, which is also added in this study to determine the values of the output parameters at different frequency inputs so that non-linearity can also be considered.

The output parameters that are selected in this optimization study to be optimized are natural frequency of the proof mass (Y_1), displacement of proof mass under and input acceleration (Y_2), pull-in voltage (Y_3), change in capacitance (Y_4) and Brownian noise equivalent acceleration (BNEA) (Y_5).

3.3 Space Filling Design Selection

Unlike physical experiments, the determination of space filling design space for computer experiments depends on two criteria. The first one is that any combination of input factors must not show up more than one time as replication is usually needed in physical experiments to

compensate errors. Secondly, the combinations of input factors must spread over the complete area for the design space, such that various behaviors of the output parameters in contrasting parts of the space can be analyzed. This reason behind because of complicated behaviour of computer experiments based simulations, the output parameter's response can vary over the design space. Based on above discussion, this leads to the selection of space filling design technique to construct our design space for MEMS dual-axis accelerometer optimization. Space filling designs have been commonly used for experimental designs based on computer experiments. Such type of designs constantly distribute the different combinations of input factors (points) all around the design space. In the list containing different types of space filling designs, Latin hypercube sampling scheme has become popular approach for designing computer experiments [91].

Latin hypercube sampling (LHS) approach, first introduced by [92], creates the design space for input factors considering two objectives: the smallest width linking any two design space points has be to be maximized, and the points equally cover the complete design space. This makes sure sufficient degree of freedom to evaluate quadratic and linear behaviours of factors and discrepancy among values is also reduced. For each design factor, the design point levels are evenly spaced between its low and high levels. The number of levels for each design factor depends on the number of runs in the design. The number of runs for simulations is selected depending on the time, cost, and resources available for conducting the computer experiment. However, for LHS and other space filling design types, it is proposed that the total number of simulation runs for computer experiment should be $10X$, where $X(=8)$ is the number of input factors.

For the DACE based optimization of MEMS dual-axis accelerometer design, Latin hypercube sampling technique is applied using JMP Pro 13 software to create design space containing the combinations of design factors as shown in Table S1 of the supplementary file. Considering the time consumed during each simulation run, the number of runs were set to 80 i.e., 10 runs per each design factor. Figure 3.1 gives a visualization of the design space for each two input factors. It must be analyzed that using LHS, the points are spaced in a way covering the entire design space and the chances to analyze different behaviors of output responses are increased.

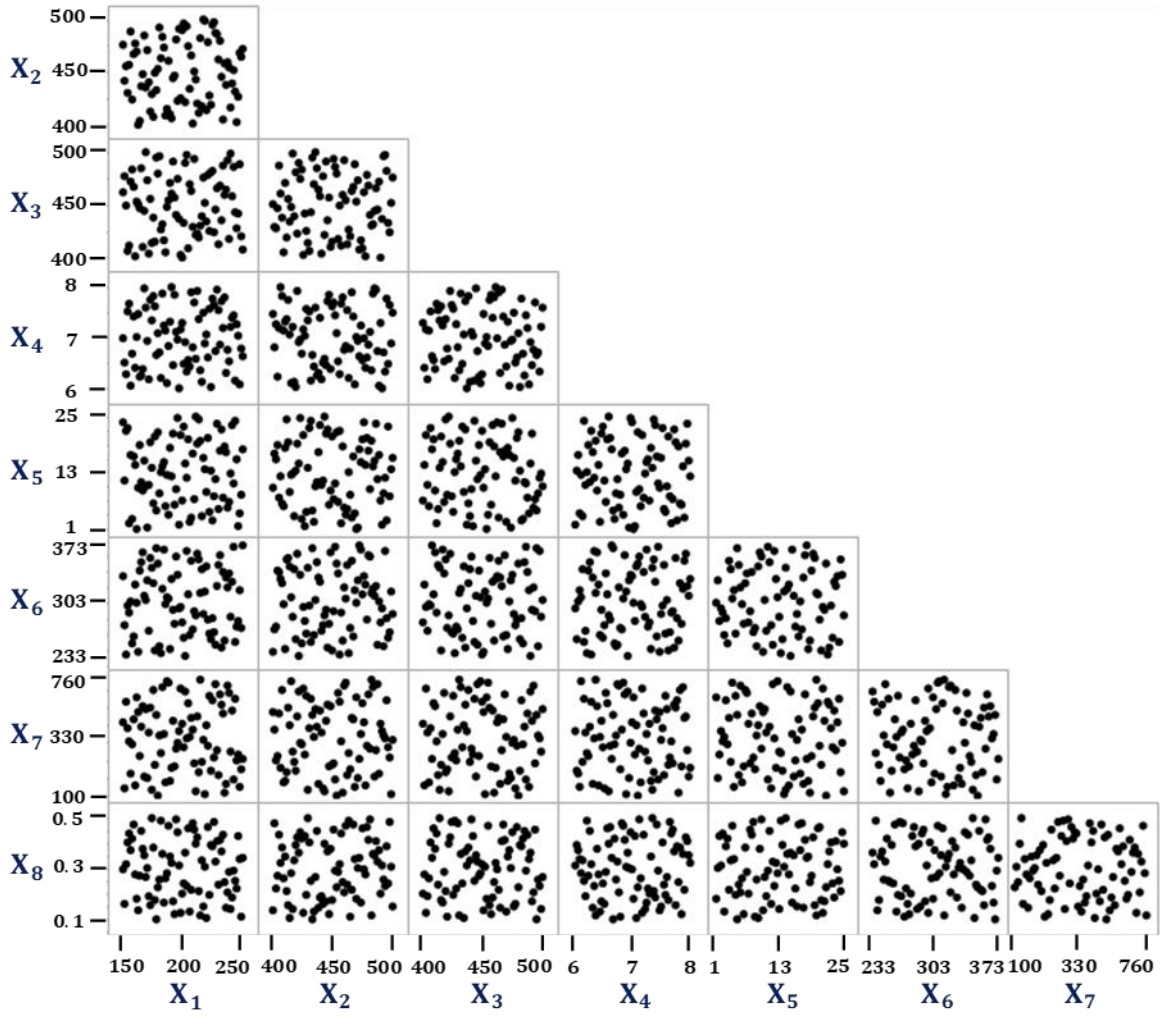

Figure 3.1: Design space to conduct computer experiment for MEMS accelerometer optimization.

3.4 Desirability Function Approach for Multi-response Optimization

The main goal of this optimization study is to optimize the five output parameters at the same time. For this a suitable technique need to be selected so that an optimal value for all these output parameters can be obtained simultaneously. Different methodologies have been presented previously to optimize more than one output parameters at same instant. These contain approaches such as loss function [93], distance function [94] and desirability function [95]. In loss function based technique, outputs are simultaneously optimized by giving the prediction in a function called loss function. In distance function, an algorithm is built in which linear dependence among various response parameters are checked and then those set of response variables are chosen having no

dependence. A function is then developed which evaluates the distance between optimum and measured value of each response.

The desirability function approach, for optimizing multiple output responses simultaneously is the widely used approach. This method was originally proposed by Harrington [96] in the shape of mathematical exponential functions and further improved by [97]. In this method, an objective function for the responses is defined, and then used to transform the estimated value of each output response to obtain its scale free value [$d_i(y_i(x))$], termed as desirability. The desirable values for d_i range from zero to one, with zero and one representing the least and most desirable values, respectively. A geometric mean of the desirabilities for each output parameter is evaluated to describe the complete desirability function. Different functional forms for desirability have been proposed in literature. The functions given by Derringer and Suich [97] accommodate non-differentiable target points and thus search methodologies may be used for optimal values. Later on, Del Castillo et al. [95] presented another function for desirability i.e., piecewise continuous functions that take care of for non-differentiable points and better algorithms such as gradient-based may be used to find optimized values for the output parameters. The desirability function is given by following:

$$d_i\big(y_i(\boldsymbol{x})\big) = \begin{cases} a_0 + b_0 y_i(\boldsymbol{x}) & if\ L < y_i(\boldsymbol{x}) \le T - \delta \\ f\big(y_i(\boldsymbol{x})\big) & if\ T - \delta \le y_i(\boldsymbol{x}) \le T + \delta \\ a_1 + b_1 y_i(\boldsymbol{x}) & if\ T + \delta \le y_i(\boldsymbol{x}) \le U \\ 0 & otherwise \end{cases} \tag{3.12}$$

where the term $\delta = (U - L)/50$ and a_0, a_1, b_0 and b_1 are constants. T, U and L are target, upper and lower values for an output parameter. The polynomial $f\big(y_i(\boldsymbol{x})\big)$ is an approximation that considers non-differentiable points and is given by following equation:

$$f\big(y_i(\boldsymbol{x})\big) = A + B y_i(\boldsymbol{x}) + C y_i(\boldsymbol{x})^2 + D y_i(\boldsymbol{x})^3 + E y_i(\boldsymbol{x})^4 \tag{3.13}$$

The overall desirability equation which is evaluated by taking geometric mean of all the desirabilities of the output parameters is as follows:

$$D(\boldsymbol{x}) = \left(\prod_{i=1}^{k} d_i^{z_i}\right)^{1/\sum z_i} = \left(d_1^{z_1} \times d_2^{z_2} \times d_3^{z_3} \times \ldots \times d_k^{z_k}\right)^{1/\sum z_i} \tag{3.14}$$

where $\boldsymbol{x}$ is the vector of input variables, k represents the total count of output parameters that need to be optimized and z_i $(0 < z_i < 1)$ depicts the significance of every output parameter with respect to other. The reason for taking geometric mean is that if any undesirable value $(d_i = 0)$ is obtained for any output response, then the overall product becomes unacceptable, and hence the condition for simultaneous optimization remains valid. It is worth mentioning here that while maximizing the value of $D(\boldsymbol{x})$ in Eq. (4.14), the goal for optimizing the output responses is to find the best combination of input factors, instead of getting the value of overall desirability, $D(\boldsymbol{x})$ equal to one.

A summary of the complete optimization methodology proposed in this work is given in the form a flowchart as illustrated by Fig. 3.2. The results for the implementation of all these steps are discussed in the next section.

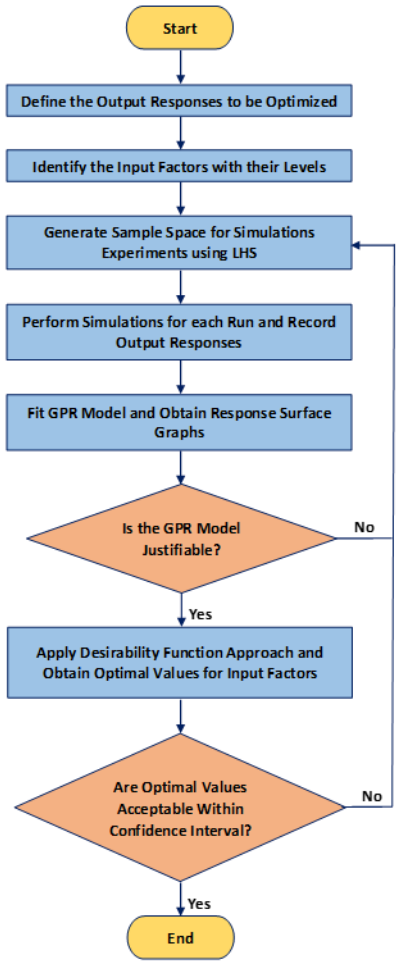

Figure 3.2: Flowchart for optimization of MEMS accelerometer based on DACE method.

Chapter 4: FEM Simulations and Results

After presenting the analytical model and a new methodology in MEMS to optimize dual-axis MEMS accelerometer design, it is followed by finite element method (FEM) modelling and simulations. Through these simulations, the efficacy of the presented optimization study is also checked in this section.

4.1 Microfabrication Process

As discussed earlier, the dual-axis accelerometer is designed to be fabricated using SOIMUMPs (Silicon On Insulator) Micromachining process, offered by MEMSCAP Inc. USA [64]. It's a Silicon on Insulator (SOI) patterning and etching process having four masks. In this process, SOI wafer is used as starting substrate with thickness of either 10 µm or 25 µm. Below this 25 µm SOI layer, oxide layer and handle wafer (substrate) of thickness 2 µm and 400 µm, respectively are present. The microfabrication process steps for the proposed MEMS accelerometer design are shown in Fig. 4.1.

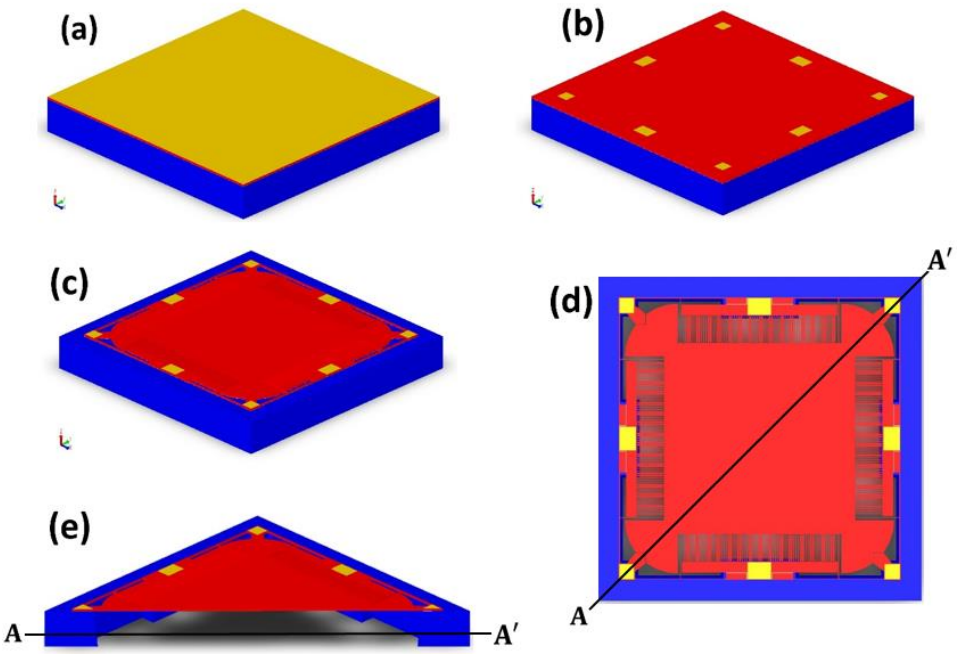

Figure 4.1: SOIMUMPs microfabrication process steps for the proposed MEMS accelerometer design.

The description of the process steps can be summarized as follows:

a) At start, there is a SOI wafer as shown in Fig. 4.1(a). The SOI layer is doped by keeping a photosilicate (PSG) layer while annealing it for 1 hour at 1050 ℃ in the presence of Argon. The PSG layer is then expelled by means of wet chemical etching.
b) The first layer that is deposited is Padmetal (consisting of 20 *nm* chrome and 500 *nm* gold stack) using lift off process as shown in Fig. 4.1(b).
c) Then the patterning of silicon is done using lithography technique while applying a second mask. The subsequent etching process is performed using Deep Reactive Ion Etching (DRIE) as shown in Fig. 4.1(c).
d) Next, a third mask level i.e., TRENCH is applied while reversing the wafer and the substrate layer (400 μm) is patterned using the lithography technique and successive etching is done using DRIE. Finally the outside layer is removed from regions defined by TRENCH layer by wet oxide etching process and the final suspended structure is obtained as shown in Fig. 4(d,e).

4.2 FEM Modelling

Various FEM analyses are conducted on the structure of the proposed MEMS accelerometer in a commercially available tool; CoventorWare® software. These analyses were carried out to estimate different output parameters that are used in Design and Analysis of Computer Experiments (DACE) based optimization against different combinations of input factors obtained from LHS sampling space. These parameters include natural frequency, mechanical sensitivity/proof mass displacement, pull-in voltage, capacitance change, Brownian noise equivalent acceleration (BNEA).

As shown in Fig. 4.2, the proof mass and suspension beams in 2-DoF accelerometer model are meshed using solid tetrahedral elements with total number of 739,599 and 272,580 elements, respectively. The suspension beams modelled based on Euler-Bernoulli beam theory and are finely meshed as compared to the proof mass. The above-mentioned output parameters, except BNEA were estimated while carrying out simulations in CoventorWare MEMS+ module. For the calculation of BNEA, damping coefficients were first estimated through simulations in DampingMM module of CoventorWare. These damping coefficients estimated at different

temperatures and pressures are also given as input for FEM simulations in CoventorWare MEMS+ module. During damping estimations, the squeeze film damping effect is modelled using Reynold's equation and is given as [98]:

$$\frac{P_a g^2}{12\mu_{eff}} \nabla^2 \left(\frac{P}{P_a}\right) - \frac{\partial}{\partial t}\left(\frac{P}{P_a}\right) = \frac{\partial}{\partial t}\frac{d}{g} \tag{4.1}$$

where P is the pressure across the combs in comparison to the atmospheric pressure P_a, g (g_1, g_2) is the width of the gap between rotor and stator combs and d is the width of the gap after the movement of the proof mass.

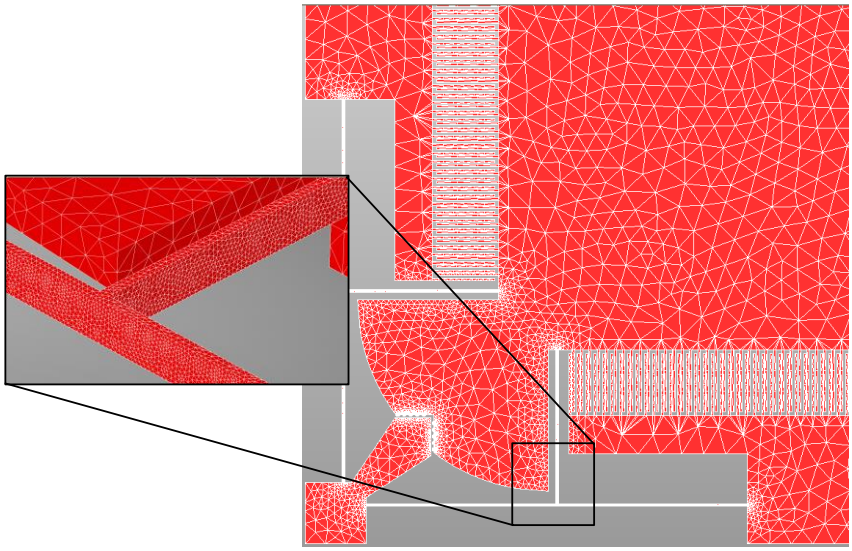

Figure 4.2: FEM meshed model for the dual-axis MEMS accelerometer design.

For the analyses in CoventorWare MEMS+ module, a systematic approach is followed; first the material data base file is created, which contains the materials with their properties to be used in the microfabrication process. These materials are then used to mimic the microfabrication process in the ProcessEditor tab while giving thickness for each material layer. Then the 3D model for the MEMS accelerometer is constructed in Innovator tab of CoventorWare MEMS+ module. The 3D components used to build the 3D model are first made available from ComponentLibrary tab and the specific material (layer) is assigned to each component. Once the 3D model is constructed, it can be used to perform FEM simulations which are done in Simulator tab of tool.

The output parameters such as natural frequency, mechanical sensitivity, pull-in voltage and capacitance change, needed for the Design and Analysis of Computer Experiments (DACE) based optimization against each combination of input factors are estimated while carrying out analyses in Simulator tab of CoventorWare MEMS+ module. This module gives the provision of carrying out Multiphysics simulations such as coupling between electrical and structural domains while carrying out electrostatic analysis. To estimate the capacitance change between combs, the 3D model created in Innovator is imported into MATLAB® Simulink and integrated with the tool. To include the effect of damping at various temperatures and pressures, the same 3D model is also built in CoventorWare Layout editor and damping coefficients are estimated using DampingMM module of tool as discussed previously.

The thickness of the SOI layer in the whole structure is 25 μm, with the mechanical properties of silicon given by SOIMUMPs microfabrication process i.e., Young's modulus of 169 GPa, density of 2500 Kg/m^3 and Poisson ratio of 0.29 [99].

4.3 Response Surface Plots for Output Parameters

To record the values of the of the output parameters recorded against each set of input factors obtained during computer experiment performed on MEMS dual-axis accelerometer design, the finite element method (FEM) simulation approach as developed and discussed in section 4.2 is utilized. After recording the values for 80 runs, Gaussian process regression (GPR) model is fitted to this data using the JMP statistical software and metamodels are obtained. Based on these metamodels effect of significant input factors on each parameter is analyzed and discussed with the help of response surface graphs. The whole data for 80 runs is recorded in the form table as given in the Table S1 of the supplementary file.

4.3.1 Dependency of Natural Frequency (Y_1) on Input Factors

The value of hyperparameter θ, for each input factor is set by minimizing the negative log of likelihood estimate based on Eq. (3.11) and are listed in Table S2 of the supplementary file. Larger the value of θ for an input factor, larger will be its impact on the output parameter. From Table S2, based on the values of θ, it is observed that the input factors X_3 (length of spring beam,

LSB-2) and X_4 (width of spring beam, WSB) have larger impact on the output response Y_1 (natural frequency) with θ values of 9.7423×10^{-5} and 0.35536, respectively. The dependency of natural frequency on X_3 and X_4 i.e., on the width and length of suspension beam (stiffness elements) is also in accordance with Eq. (2.7).

For the output response Y_1 (natural frequency), the two-factor interactions are also given in Table S2. It is observed that the input factors X_3 (length of spring beam, LSB-2) and X_4 (width of spring beam, WSB) have the highest interaction value of 0.0046 to cause a change in the value of Y_1 (natural frequency). The effect of interaction X_3X_4 on Y_1 can be further observed with the help of 3D response surface plot shown in Fig. 4.3, while keeping the values for other input factors at their mean levels. The plot shows that the value Y_1 (natural frequency) can be decreased by increasing LSB-2 and decreasing (WSB). Furthermore, the change in the value of Y_1 is more sensitive to change in WSB as compared to LSB-2. When the width of spring beam, WSB is 6 μm, then change in natural frequency is less affected by the change in length of spring beam, LSB-2 as compared to when the width of spring beam is 8 μm.

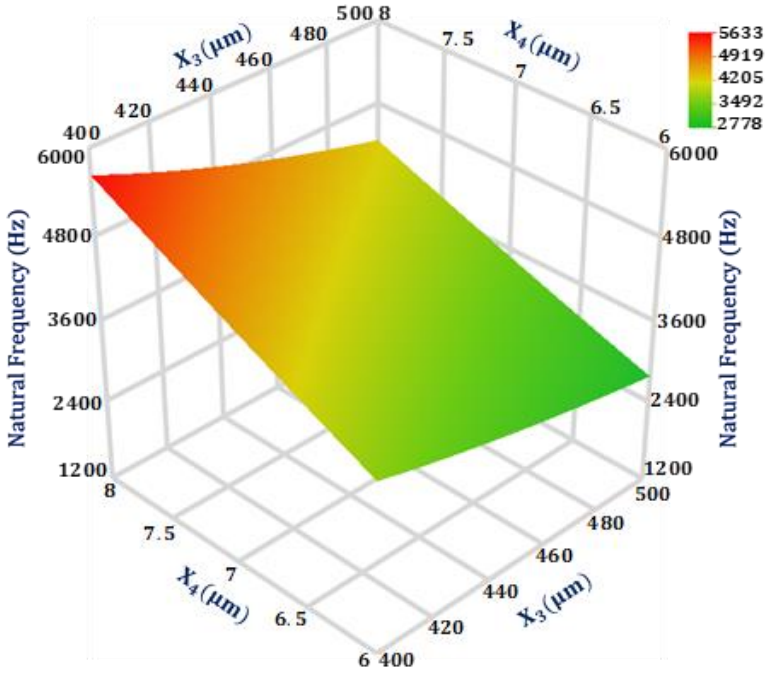

Figure 4.3: 3D response surface plot showing interaction between LSB-2 and WSB for natural frequency.

4.3.2 Dependency of Proof Mass Displacement (Y_2) on Input Factors

For each input factor, the value of hyperparameter θ, obtained after minimizing the negative log of likelihood from Eq. (3.11) are given in supplementary Table S3. The results show that the value of proof mass displacement is significantly dependent on X_4 (width of spring beam, WSB), X_5 (input acceleration, IA) and X_8 (frequency ratio, FR) with values for hyperparameter θ as 0.335, 0.0055 and 1.2415, respectively. The dependency of proof mass displacement on input acceleration, frequency ratio (ω/ω_n) and width of suspension beam (stiffness element) also satisfies Eq. (2.3).

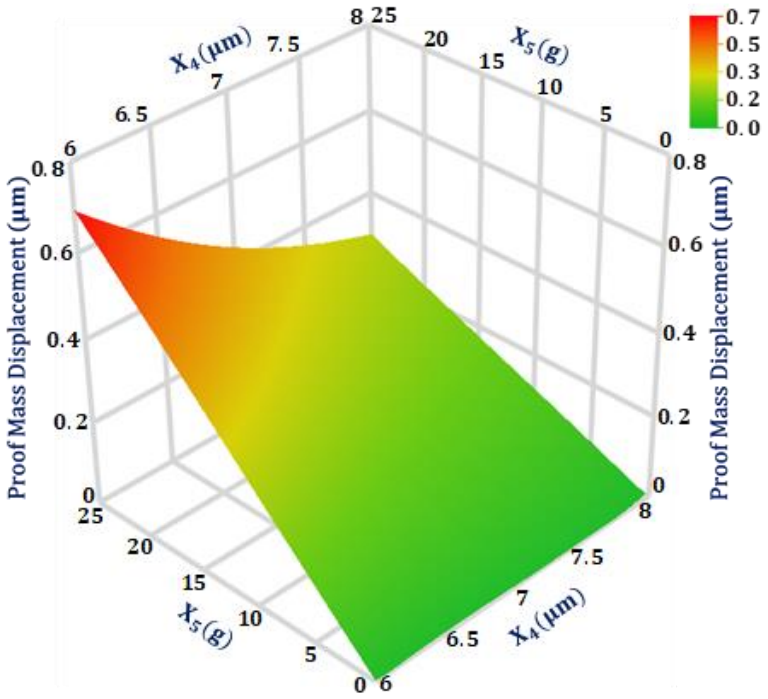

Figure 4.4: 3D response surface plot showing interaction between WSB and IA for proof mass displacement.

In Supplementary Table S3, the two factor interactions are also listed for the output response proof mass displacement (Y_2). The maximum interaction is obtained between X_4 (width of spring beam, WSB) and X_5 (input acceleration, IA) with value of 0.031. This interaction can be analyzed using 3D response surface graph as shown in Fig. 4.4. The values of other input factors are kept at their mean levels. The graph shows that the proof mass displacement can be increased

by decreasing width of suspension beam and increasing input acceleration. The change in proof mass displacement is more sensitive to change in input acceleration as compared to width of suspension beam. Moreover, the change in proof mass displacement is more sensitive than change in width of suspension beam, when input acceleration is 25 g, as compared to lower values of input acceleration.

4.3.3 Dependency of Pull-in Voltage (Y_3) on Input Factors

The impact of each input factor on the output parameter Y_3 (pull-in voltage) is obtained by estimating its hyperparameter θ, after minimizing the negative log of likelihood using Eq. (3.11) and the results are given in supplementary Table S4. The value of pull-in voltage is significantly dependent on X_1 (comb overlap length, COL), X_4 (width of spring beam, WSB) and X_8 (frequency ratio, FR). The dependency of pull-in voltage on overlap length and width of suspension beam is also in compliance with Eq. (2.11).

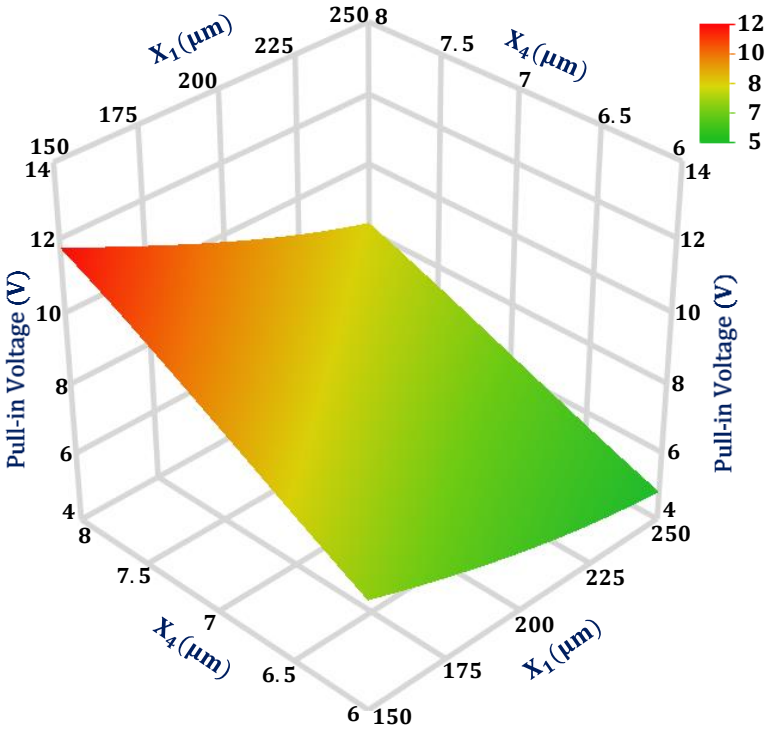

Figure 4.5: 3D response surface plot showing interaction between COL and WSB for pull-in voltage.

The interactions between the input factors for the output parameter Y_3 (pull-in voltage) are listed in supplementary Table S4. The maximum value of interaction is obtained as 0.00422, between input factors X_1 (comb overlap length, COL) and X_4 (width of spring beam, WSB). This interaction is further analyzed with the help of 3D response surface plot as shown in Fig. 4.5, with values of other input factors at their mean levels. It can be depicted from the plot that the value of Y_3 (pull-in voltage) can be increased with the increase in WSB (width of spring beam) and decrease in COL (comb overlap length). The change in pull-in voltage is more sensitive to width of suspension beam as compared to overlap length. Furthermore, when the width of suspension spring is 8 μm, the pull-in voltage is more affected due to the change in overlap length as compared to when the width of suspension spring is 6 μm.

4.3.4 Dependency of Capacitance Change (Y_4) on Input Factors

Supplementary Table S5 (given in supplementary file) shows the list of values for hyperparameter θ for each input factor that are obtained through minimizing the negative log of likelihood using Eq. (3.11). For the output parameter Y_4 (capacitance change), the input factors that have significant effect on its value are X_4 (width of spring beam, WSB), X_5 (input acceleration, IA) and X_8 (frequency ratio), with θ values of 0.1235, 0.0019 and 0.8767, respectively. Based on Eq. (2.3) and (2.10), the dependency of capacitance change on width of spring beam, input acceleration and frequency ratio are also satisfied.

The two-factor interaction between the input factors that cause a change in the value of Y_4 (capacitance change) are also given in supplementary Table S5. Among these values, the two-factor interaction between X_4 and X_5 is found to have maximum value of 0.0381 which is further analyzed through 3D response surface graph as shown in Fig. 4.6. The graph shows that value of capacitance change increases on increasing the value of input acceleration and decreasing the width of spring beam. Moreover, the change in value of capacitance change is more sensitive to IA and in addition the change in its value more affected due to the change in WSB when IA=25 g, as compared to when IA is less than 25 g.

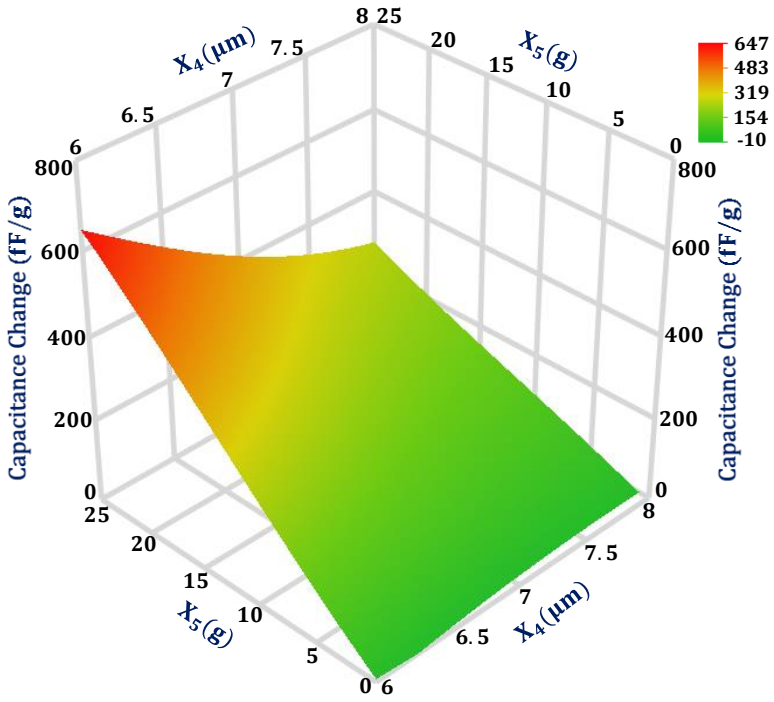

Figure 4.6: 3D response surface plot showing interaction between WSB and IA capacitance change.

4.3.5 Dependency of BNEA (Y_5) on Input Factors

After minimizing the negative log of likelihood estimate using Eq. (3.11), the values for hyperparameter θ are obtained, which show the comparative effect of each input factor on the output response BNEA and are listed in supplementary Table S6. The results show that the value of BNEA is significantly affected by X_1 (comb overlap length, COL), X_6 (temperature, T) and X_7 (pressure, P). The obtained θ values for these input factors are 0.000142, 5.2549×10^{-5} and 6.0283×10^{-6}, respectively. The dependency of BNEA on temperature and pressure agrees with Eq. (2.12).

In Supplementary Table S6, the two-factor interaction values are also listed to analyze the effect on BNEA due to the change in the input factors. Among these interaction values, the maximum interaction is found between temperature, pressure and comb overlap length, pressure with values of 0.007235 and 0.007285, respectively. This interaction can be analyzed using 3D response graph, shown in Fig. 4.7. Smaller the value of temperature and pressure, smaller will be the value of BNEA. The change in BNEA is more sensitive to pressure as compared to temperature

as illustrated in Fig. 4.7(a). However, the change in BNEA is more affected due to the change in temperature when pressure is 760 Torr, as compared to the pressure value at 100 Torr. Similarly, as shown in Fig. 4.7(b), the value of BNEA increases due to the increase in comb overlap length (COL) and pressure (P). Moreover, a linear relation of BNEA with COL can be observed.

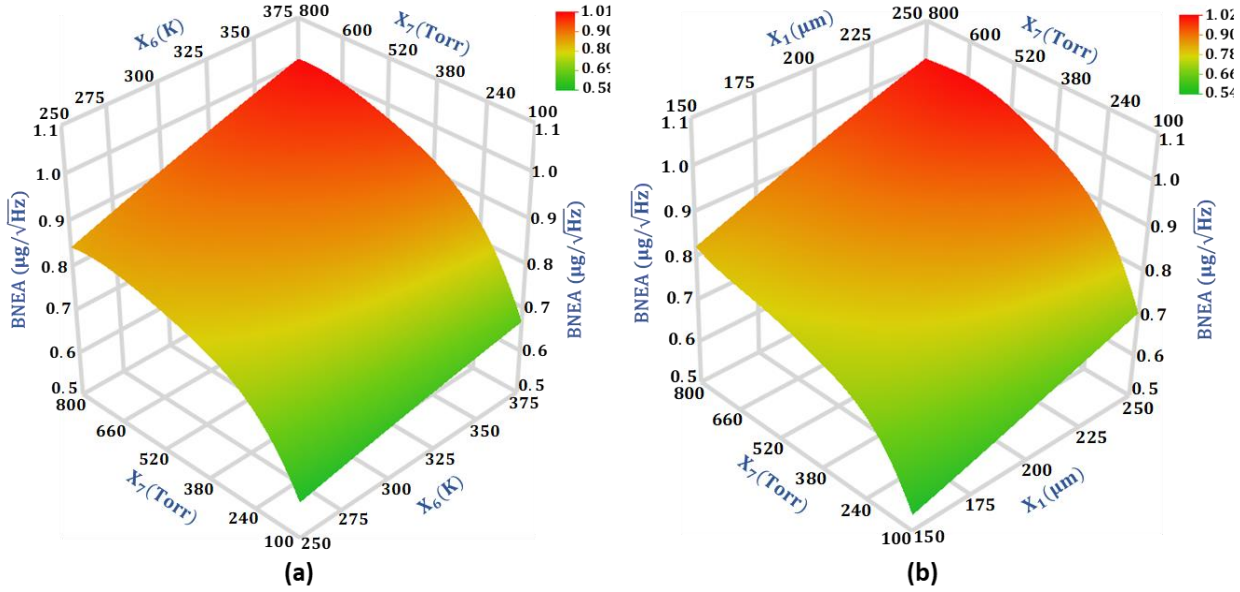

Figure 4.7: 3D response surface plot showing interaction between (a) Pressure and Temperature and (b) COL and Pressure for BNEA.

4.4 Optimization Results

4.4.1 Objective Function for Optimization

The optimization of proposed MEMS dual-axis accelerometer involves minimizing the natural frequency, BNEA and maximizing proof mass displacement, capacitance change and pull in voltage while considering few constraints. The objective function is defined as:

Maximize – Proof mass displacement
Maximize – capacitance change
Minimize – Natural frequency (4.2)
Minimize – BNEA
Maximize – Pull-in Voltage

such that:

$150\ \mu m \leq OL \leq 250\ \mu m$

$400\ \mu m \leq LS\text{-}1 \leq 500\ \mu m$

$350\ \mu m \leq LS\text{-}2 \leq 500\ \mu m$

$6\ \mu m \leq WS \leq 8\ \mu m$

$IA = 25$ g

$P = 760$ Torr

$T = 300\ K$

$0.1 \leq FR \leq 0.5$

In the above defined objective function, the values of input factors pressure (P) and temperature (T) are kept at room conditions because the proposed accelerometer is desired to work in this environment. Moreover, the value of input acceleration (IA) is set at 25 g, since it is intended to test the accelerometer at maximum desired acceleration.

4.4.2 Optimal Values through Desirability Function

After developing the GPR based regression metamodels for each output parameter and defining the objective function as given by Eq. (4.2), the next goal is to optimize this function. For the simultaneous optimization of all the output parameters, the desirability function based approach is used.

Two methods have been commonly used to optimize the desirability function i.e., search methods (e.g., Hooke-Jeeves method as given by Derringer and Suich [97]) and gradient-based methods (e.g., generalized reduced gradient (GRG) algorithm). The former method is a derivative-free approach and can be applied for optimization of objective functions where derivative does not exist. The later approach requires optimization functions to have continuous first derivatives but is more efficient and widely used method in industries [95]. The optimization of the objective function for the proposed MEMS dual-axis accelerometer design is achieved using gradient descent algorithm. The obtained optimal values for the input factors (except temperature and pressure) are shown in Fig. 4.8.

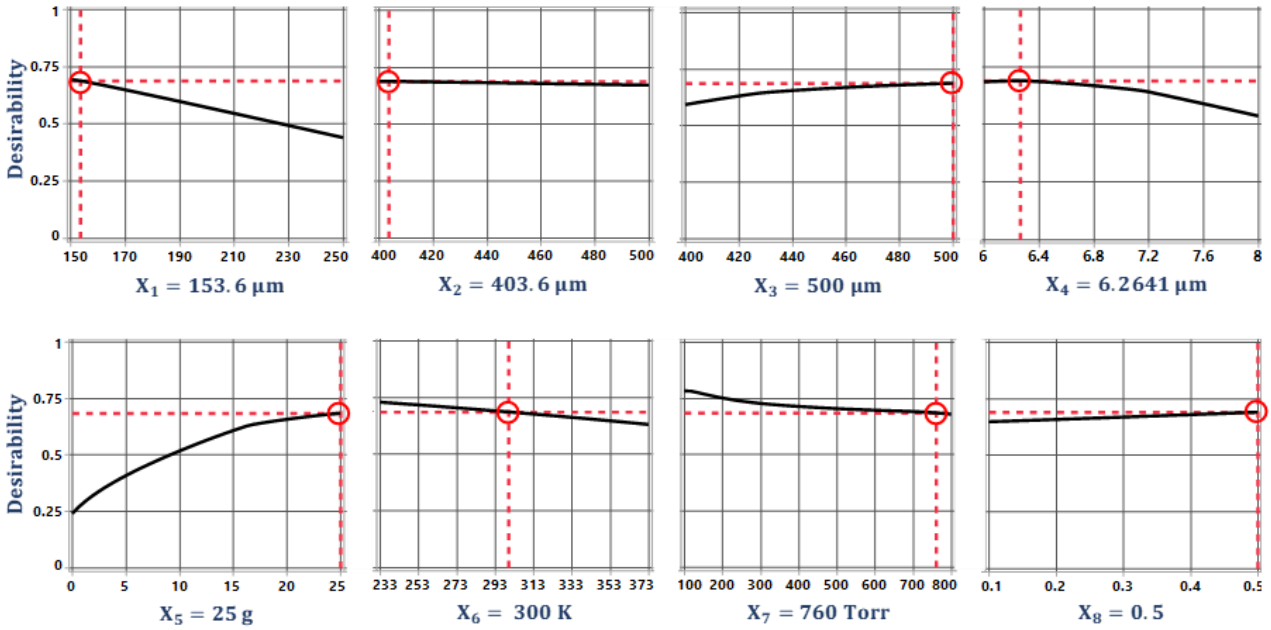

Figure 4.8: The optimal values of the input factors for MEMS dual-axis accelerometer design.

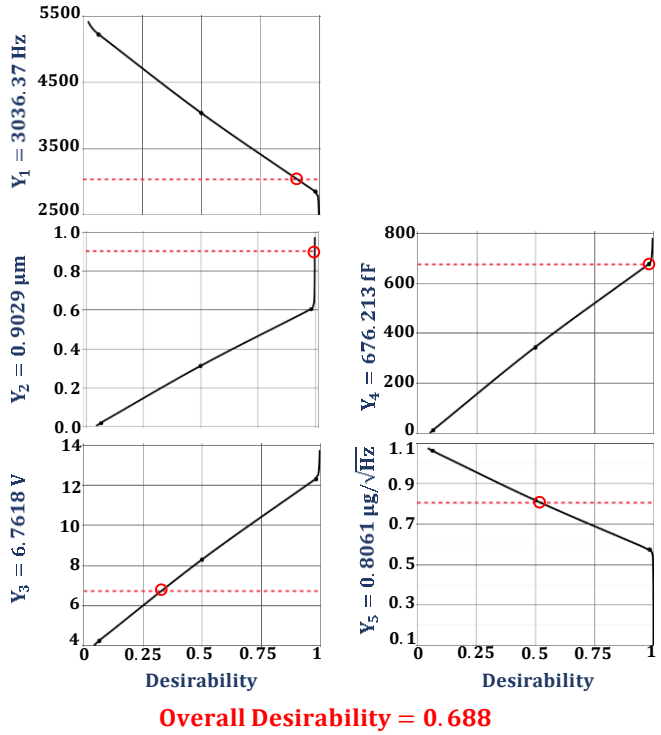

Figure 4.9: The predicted optimal values of the output parameters based on optimal input factors.

Figure 4.9 shows the predicted optimized values of output parameters for MEMS dual-axis accelerometer design based on the optimized values of input factors shown in Fig. 4.8. The overall

desirability value obtained is 0.688 predicting natural frequency of 3036.37 Hz, displacement of 0.9029 μm for proof mass, pull-in voltage of 6.7618 V, 676.213 as change in capacitance and BNEA of 0.8061 $\mu g/\sqrt{Hz}$.

4.5 Predicted Output Parameters Verification

The predicted optimal values presented in previous section are verified using the same computer based FEM simulations that were used in the experiment to check if the optimal values lie within the 95% confidence interval.

4.5.1 Modal Analysis

Figure 4.10 shows the first three mode shapes obtained from the modal analysis, performed in CoventorWare MemMech module to compare the natural frequency with the predicted one. The

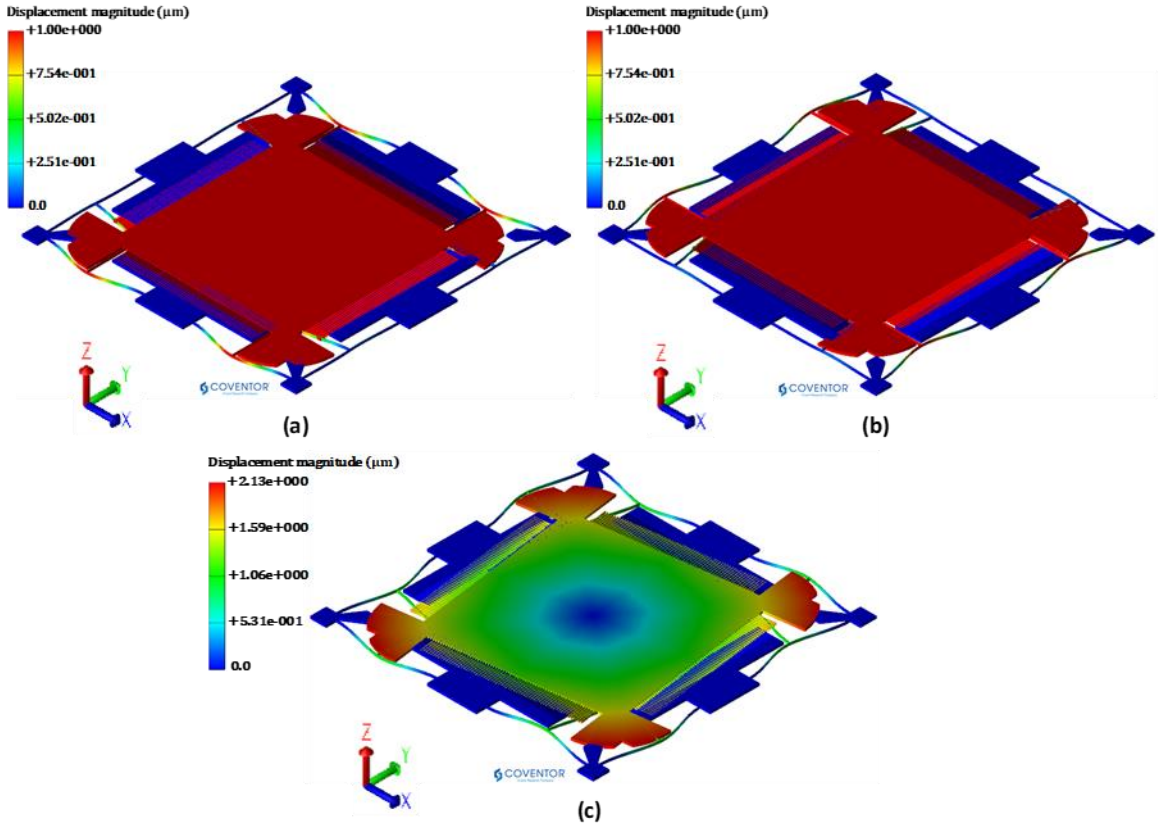

Figure 4.10: Natural mode shapes for MEMS dual-axis accelerometer (a) 1st mode along y-direction 3038.133 Hz, (b) 2nd mode along *x*-direction 3038.133 Hz and (c) 3rd mode about *z*-direction 3925.195 Hz.

first and second modes have natural frequency of 3038.133 Hz with translational displacement of the proof mass along *x* and *y* axes as shown in Figs 4.10(a) and 4.10(b). The third mode is torsional about *z*-axis, as shown in Fig. 4.10(c) and has a frequency of 3925.195 Hz. This also depicts that the required first two modes are well separated from third mode in term of their frequency values. The natural frequency of 3038.133 Hz obtained through simulation is in good correspondence with the predicted value and lies within the 95% confidence interval i.e., $3036.98 \leq 3038.13 \leq 3039.89$.

4.5.2 Harmonic Analysis

Figure 4.11 shows the frequency response curve for the MEMS accelerometer at 25 g obtained using CoventorWare. The results show a close agreement both in resonant frequency and proof mass displacement amplitude. The results show that at maximum value of input acceleration i.e., 25 g and at room temperature and pressure conditions, the displacement in the proof mass is 185.5 µm at resonant frequency. This value is much higher than the initial air gap of 2.5 µm between the stator and rotor combs of the MEMS accelerometer. However, at the predicted value of frequency ratio (FR=0.5), the displacement amplitude of the proof mass is 0.898 µm, which is in good correspondence with the predicted value of 0.9029 µm and lies within the 95% confidence prediction interval i.e., 0.888 µm ≤ proof mass displacement ≤ 0.919 µm. Moreover, considering

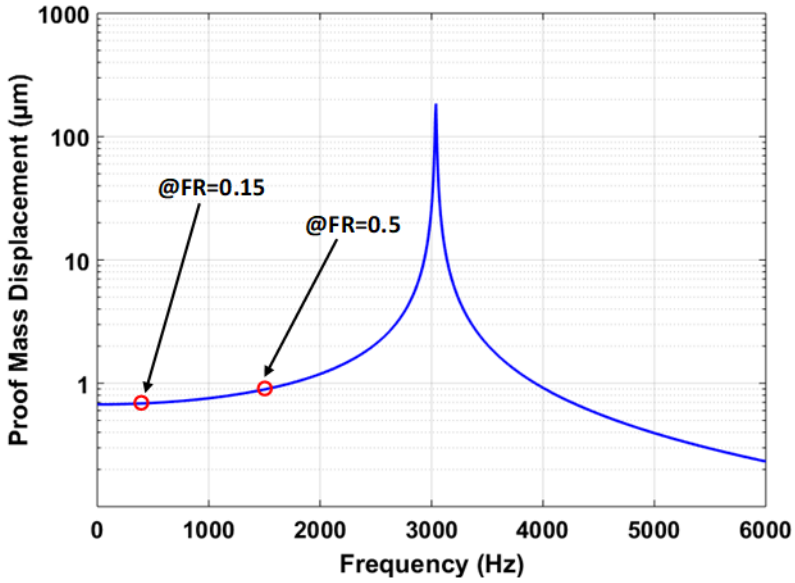

Figure 4.11: Frequency response curve of the MEMS accelerometer proof mass under 25 g.

the constraints for the operation of non-resonant MEMS capacitive accelerometer, the operational bandwidth region must be linear. This constraint calls for limiting the frequency ratio (FR) value at 0.15, the point at which the frequency response curve in Fig. 4.11 maintains a linear behavior, thus giving us a bandwidth region of 0-450 Hz for the operation of MEMS dual-axis accelerometer design. The observed value of the proof mass displacement in bandwidth region is 0.688 µm.

4.5.3 Analysis for Pull-in Voltage

To verify the value of pull-in voltage obtained from desirability function, an analysis is done in CoventorWare MEMS+ to obtain a graph for proof mass displacement against biasing voltage as shown in Fig. 4.12. The graph depicts that the phenomenon of pull-in occurs at an applied voltage of 6.788 V and shows a good agreement with predicted one i.e., 6.7618 V. the obtained value also lies in the 95% confidence interval: 6.444 V ≤ 6.788 ≤ 6.998 V.

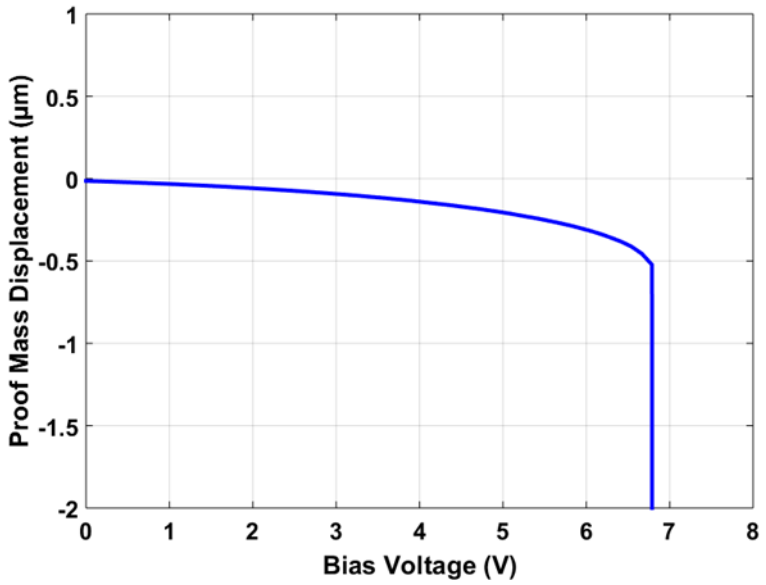

Figure 4.12: Displacement in proof mass due to applied bias voltage across combs.

4.5.4 Verification of Capacitance Change

For the analysis of capacitance change to verify the predicted value, the CoventorWare MEMS+ module is interfaced with Simulink tool of MATLAB. A voltage difference of 2.25 V is created between electrodes since the mechanical part of the design has to be interfaced with suitable electronics to convert capacitance change into voltage, which is MS3110 [100] for our

case having requirement of 2.25 V. The accelerometer is given an input signal of magnitude 25 g, at an oscillating frequency of 1519 Hz (FR=0.5), as shown in Figure 4.13(a). This causes a change in the value of gap and antigap capacitance as illustrated in Figs. 4.13(b) and 4.13(c) respectively. Due to the change in these capacitance values, a capacitance change equal to 694 fF is obtained. This value is in good agreement with the predicted capacitance change of 676.213 fF and lies within the 95% confidence prediction interval i.e., 617.226 fF $\leq$ 694 fF $\leq$ 734.438 fF. As discussed in frequency response analysis section, the working of the accelerometer is limited to frequency ratio of 0.15 due to requirement for its linear operation, so the value of capacitance change is also estimated at 450 Hz i.e., within the bandwidth region and results are shown in Fig. 4.14. The results show that under an acceleration of magnitude 25 g and at frequency of 450 Hz, a change in capacitance of 523 fF is obtained within the linear bandwidth region.

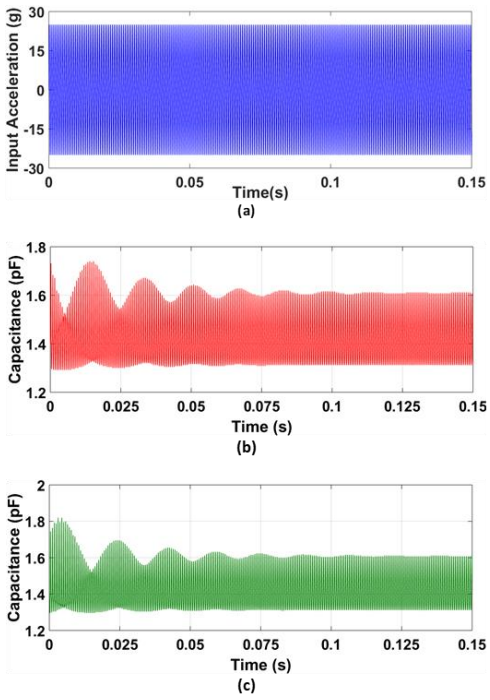

Figure 4.13: Analysis for capacitance change at predicted value of frequency ratio; (a) input acceleration; (b) change in gap capacitance; (c) change in anti-gap capacitance.

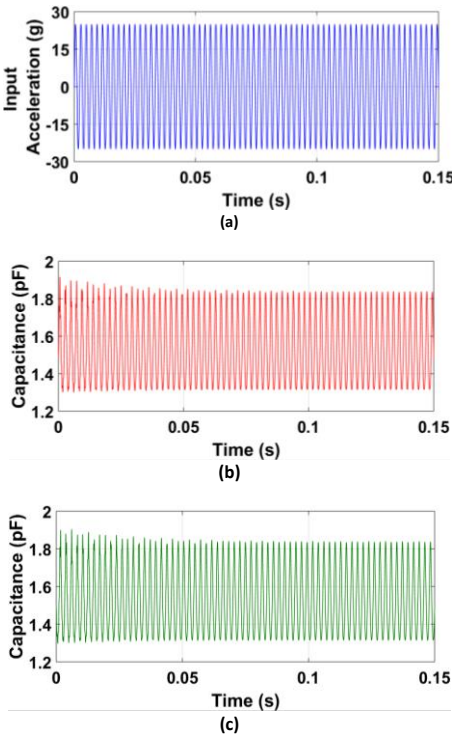

Figure 4.14: Analysis for capacitance change within the bandwidth region (a) input signal, (b) sensing gap capacitance, (c) anti-gap capacitance.

4.5.5 Verification of BNEA

To verify the predicted optimized value of Brownian noise equivalent acceleration (BNEA), damping coefficients for slide and squeeze film damping are estimated first using DampingMM module of CoventorWare software 300 K and 760 Torr. After the coefficients are estimated, the value of BNEA is evaluated based on optimal value of factors and using Eq. (2.12). The obtained value is 0.8054 $\mu g/\sqrt{Hz}$, close to the 0.8061 $\mu g/\sqrt{Hz}$; being predicted by desirability function and remain in the 95% confidence interval; 0.7901 $\mu g/\sqrt{Hz} \leq 0.8054\ \mu g/\sqrt{Hz} \leq 0.8221\ \mu g/\sqrt{Hz}$.

4.6 Mechanical Displacement and Capacitance Change

For the final design, proposed in this paper based on the obtained optimal values of input factors and output responses, it is important to estimate the mechanical and capacitance cross-axis sensitivities during the operation of the accelerometer under an input acceleration. Also, the change in the value of proof mass displacement and capacitance change also need to be analyzed.

Mechanical cross axis sensitivity is due to the movement of the proof mass in the orthogonal direction with an input acceleration in the sense direction. Figure 4.15 shows the change in the proof mass displacement in both *x* and *y* directions with acceleration magnitude ranging from -25 g to $+25$ g along x-direction. The plot shows that the change in the displacement of the proof mass is perfectly linear in this range and from the slope of the graph for *x*-axis displacement, mechanical sensitivity of 0.0275 µm is obtained. The cross-axis sensitivity of proof mass along *y*-axis due to input acceleration in the x direction is 0.0002 % only.

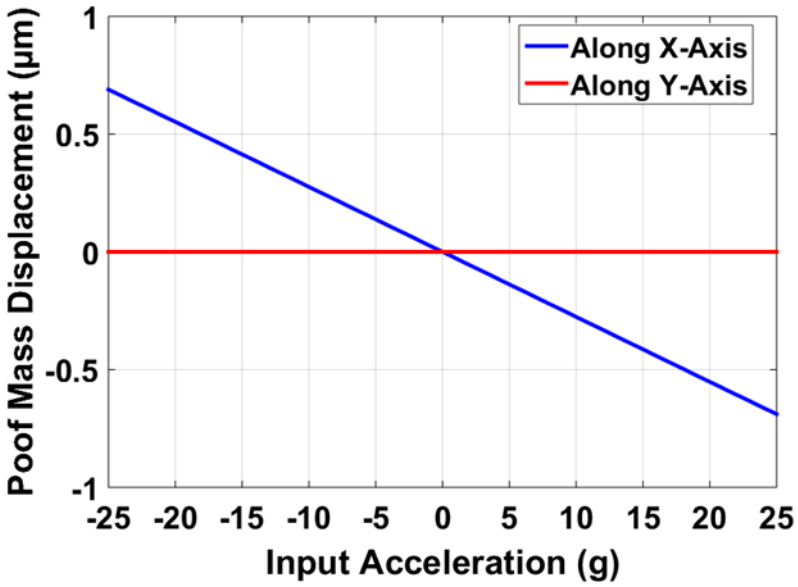

Figure 4.15: Input acceleration (*x*-direction) vs. proof mass displacement for range -25 g to +25 g (CoventorWare).

As discussed earlier, a capacitance change occurs in the sensing axis due to the change in gap between the rotor and stator combs with the displacement of the proof mass corresponding to an input acceleration. However, there is also an unwanted capacitance change in anti-sensing axis due to the change in overlap area between the stator and rotor combs, which is termed as cross-axis capacitance. Figure 4.16 shows the change in capacitance in the sensing axis (*x*-axis) along with the change in cross-axis capacitance (along *y*-axis) for acceleration range of -25 g to $+25$ in the x direction. The graph shows that the change in capacitance is nearly linear and from the slope of the fitted regression line, capacitance sensitivity of 20.4 fF/g is estimated. The resulting capacitance cross-axis sensitivity is 0.028 %. The value of cross-axis cross results in a mixed signal at the input of interface circuit. This requires additional electronic techniques like frequency

division multiplexing to extract the desired signal [101]. The resulted circuit noise equivalent acceleration (CNEA) based on Eq. (2.13) is estimated to be 0.196 $mg/\sqrt{Hz}$.

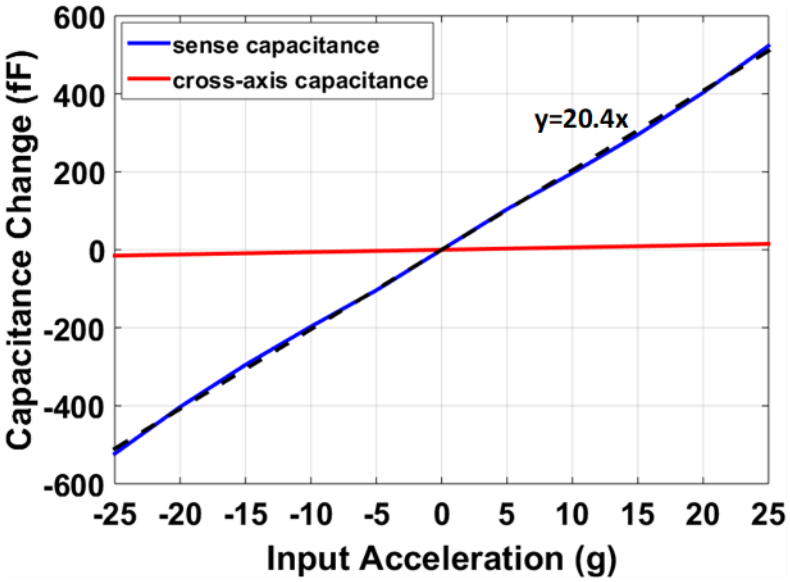

Figure 4.16: Input acceleration (*x*-direction) vs. capacitance change from -25 g to +25 g (CoventorWare).

4.7 Integration of Readout Electronics with MEMS Accelerometer Model

For MEMS accelerometers, that utilize capacitive transduction mechanism to sense input acceleration, the signal output is weak, which requires a capacitance reading circuit design to convert the output capacitance change into suitable voltage form and thus resolution can also be increased. For this purpose, the proposed MEMS dual-axis accelerometer is assumed to be interfaced with a capacitance change to voltage conversion, Universal Readout IC™ MS3110 [100]. This integrated circuit is capable of estimating both differential and single capacitors outputs and can measure capacitance change as low as 4 $aF/\sqrt{Hz}$. Figure 4.17 illustrates the integration of MEMS dual-axis accelerometer design with MS3110. A simplified block diagram is attached with MATLAB Simulink module of accelerometer design which is imported from CoventorWare MEMS+.

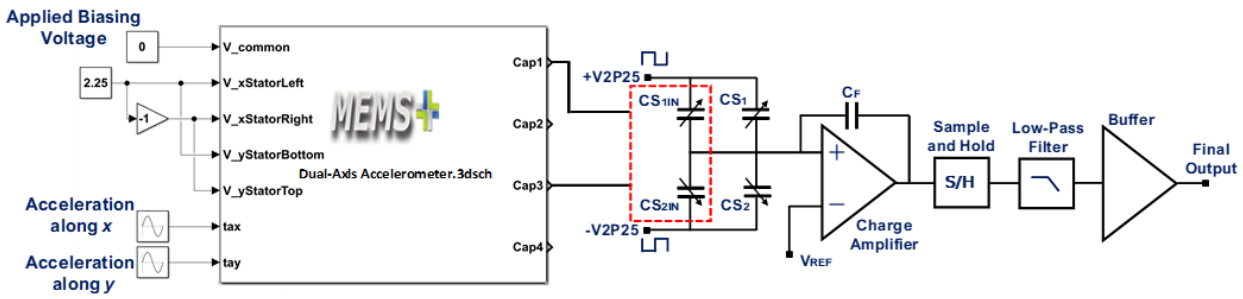

Figure 4.17: Block diagram illustration for integration of the MEMS accelerometer CoventorWare MEMS+ model with MS3110 IC.

The functioning concept of this readout for the estimation of differential based capacitance change is centered on charge amplification, then sample and hold. This is followed by a low-pass frequency filter and finally a buffer amplifier. For biasing, 2.25 V are applied between stator and rotor combs. With an input acceleration along *x*-axis, the capacitance change between output terminals Cap1 and Cap3 of the MEMS+ model and with an input acceleration in *y*-axis, the capacitance change between the output terminals Cap2 and Cap4 of the MEMS+ model are given as an input to the MS3110 IC. However, to explain the working, the circuit block diagram to measure capacitance change for acceleration along *x* is considered only. Two capacitors CS_{1IN} and CS_{2IN} represent the capacitance input from MEMS accelerometer and are thus equal to Cap1 and Cap3 respectively. To nullify the capacitance mismatch between these two input capacitors, the values of the capacitors CS1 and CS2 can be adjusted. Ideally, if there is no capacitance mismatch, then the difference $CS_1 - CS_2$ is zero. A square wave amplitude V2P25 is given as an input to MS3110. The output voltage produced by MS3110 is in the range of 0.5 to 4 V. The transfer function to find the output voltage of the MS3110 is given by:

$$V_{out} = 1.14 \times G \times V2P25 \times \frac{2\Delta C}{C_F} + V_{ref} \tag{4.3}$$

where the buffer gain G has the value of 2; $V2P25$ and V_{ref} are set to 2.25 V; ΔC is the change in capacitance ($CS_{1T} - CS_{2T}$); $CS_{1T} = CS_{1IN} + CS_1$; $CS_{2T} = CS_{2IN} + CS_2$. Suppose that there is zero mismatch between the capacitances that take input, so the term $CS_1 - CS_2 = 0$ and ΔC will only be equivalent to the difference of the capacitances Cap1 and Cap3, obtained from analysis for capacitance change. The capacitor C_F (=3.2 pF) is the feedback capacitor and its value can be adjusted to program the gain of the charge amplifier and to limit the voltage output from 0.5 to 4

V. Moreover, the buffer amplifier gain and the frequency bandwidth of the low pass filter can also be programmed. For the proposed MEMS accelerometer, the output voltage is obtained for an acceleration of −25 g to +25 g, as illustrated in Fig. 4.18. The graph shows that the obtained output voltage is within the measurement limits i.e., 3.93 V for +25 g and 0.573 V for −25 g. Moreover, a voltage sensitivity equivalent to 65.4 mV/g is obtained for final optimized MEMS accelerometer design.

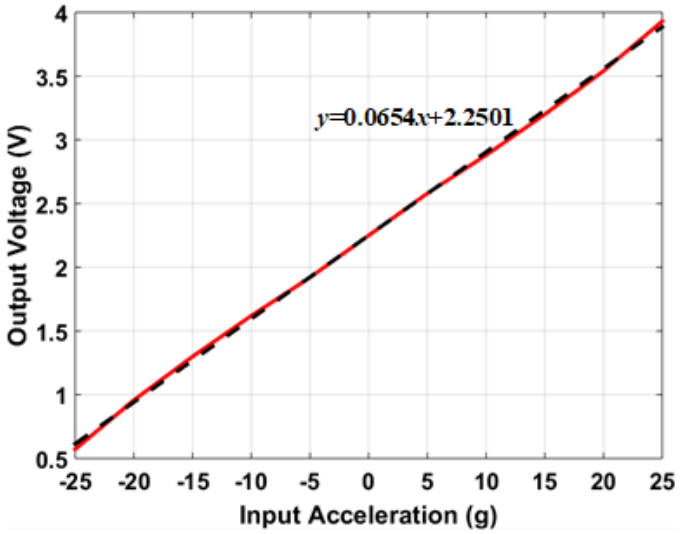

Figure 4.18: Output voltage vs. input acceleration graph obtained from MS3110 model.

Chapter 5: MEMS Capacitive Accelerometer Design II

As a supplemental part of this work, a design of capacitive MEMS accelerometer is also developed and analyzed while taking care of limitations and constraints of commercial process. Few basic analyses are performed on this proposed design to verify its working and performance.

5.1 Schematic of the Proposed Design II

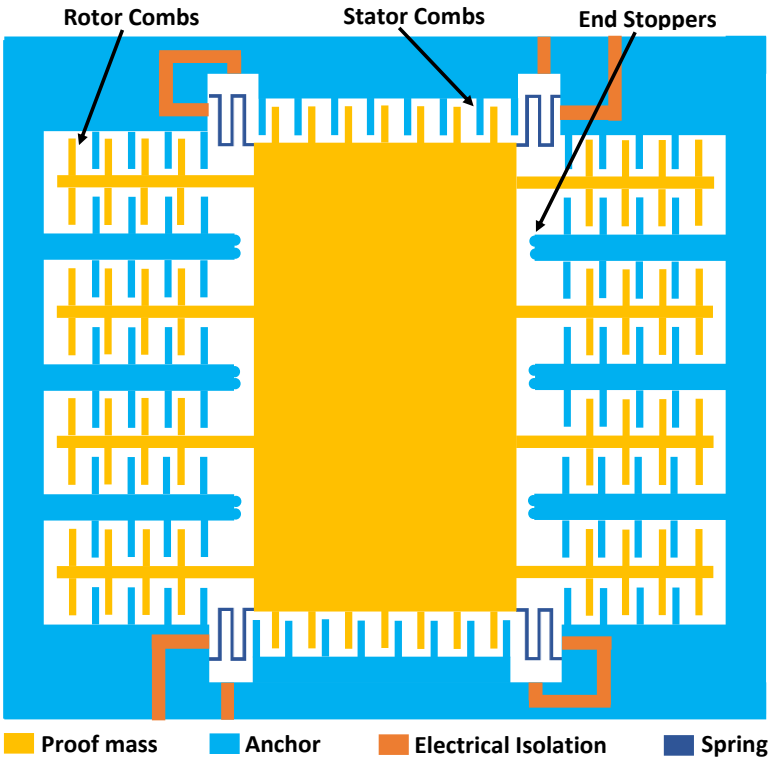

Figure 5.1: Visual representation of proposed capacitive MEMS accelerometer design II.

Figure 5.1 shows the single proof mass based single axis electrostatic MEMS accelerometer using the rules given by SOIMUMPs commercial microfabrication foundry. The design of one proof mass in the center which is hanged over the substrate using serpentine shaped mechanical springs. The other end of these springs is connected to the anchors of the respective side. Following the limitations of the process, anchors are kept outside and to make different electrodes i.e., to make separation between two electrical units, electrical isolation is used as shown in the schematic in Fig. 5.1. To sense the mechanical movement of the proof mass as a result of

input signal which is acceleration, topology of rectangular shaped combs is deployed. These combs are again designed in gap and anti-gap arrangement. To decide the ratio of gaps for this arrangement, the width of larger gap is kept equal to 3.45 times of the smaller gap, as obtained in optimization study presented by Mohammed et al. [44]. Unlike designs reported previously in literature [44, 66, 69] which utilize single proof mass and to sense its movement, combs are attached along the edge of the proof mass in one direction only to generate a capacitance change. However, greater the number of comb pairs, greater will the capacitance output. So, in order to enhance the capacitance output, this design also utilizes the other two edges of the proof mass while designing rectangular branch segments on which additional combs are incorporated. To prevent the damage of the design in case of motion of proof mass beyond its limit, round stoppers are also designed. The analytical model to determine the motion amplitude of the proof is the same as given by Eqs. (2.1)-(2.3) in Chapter 2 of this work. For damping calculations, the same analytical equations can also be utilized as given in section 2.6. The summary for the dimensions of the proposed design is given in Table 7 shown below:

Table 7: Dimensions for various parameters of the proposed MEMS design

Parameter	Value
Thickness for structural layer (t)	25 µm
Mass value of Proof mass	4.754×10^{-7} Kg
Dimensions of the proof mass ($l_m \times w_m$)	3000 µm × 2000 µm
Rectangular branch segment ($l_b \times w_b$)	1000 µm × 50 µm
Total combs (n_c)	670
Comb length (l_c)	300 µm
Overlap length between combs (l_o)	290 µm
Width for larger sensing gap (d_2)	12.075 µm
smaller sensing gap width (d_1)	3.5 µm
End stopper (radius)	3 µm
Mechanical spring width (w_s)	14 µm
Mechanical spring length (l_s)	405 µm

5.2 Analytical model for Mechanical Spring

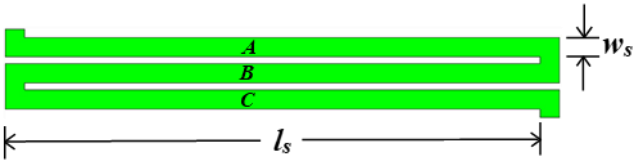

Figure 5.2: schematic for mechanical spring.

As discussed above, a serpentine shaped mechanical spring is used to suspend the central proof mass. An analytical equation to determine the equivalent stiffness k_e of the spring shown in Fig. 5.2 is required which is developed using the methodology of series and parallel combination of springs. Four similar springs are used with the proof mass and in each of them consist of three microbeams connected in series which are labelled as *A*, *B* and *C*. The equation to find stiffness of microbeams can be written as:

$$\frac{1}{k_1} = \frac{1}{k_A} + \frac{1}{k_B} + \frac{1}{k_C} \tag{5.1}$$

$$k_1 = \frac{Etw_s^3}{3l_s^3} \tag{5.2}$$

where k_1 represents the stiffness of one of the four springs, E is the Young's modulus of silicon, t is the thickness of silicon structural layer, l_s and w_s are the length of width of each microbeam, respectively. Since, all the four springs are in parallel combination, so the equivalent stiffness can evaluated using [68]:

$$k_e = 4k_1 = \frac{4Etw_s^3}{3l_s^3} \tag{5.3}$$

5.3 FEM simulations and Results

The rest the work for design II consists of estimating various performance parameters using FEM simulations and representation of their results. The simulations are done in commercially available softwares; CoventorWare® and MATLAB® Simulink.

5.3.1 Analysis for Natural Frequency

To find out the mode shapes and the values for natural frequency of the proposed design, modal analysis is carried out on the system in CoventorWare tool. Figure 5.3 depicts the first two obtained mode shapes for this design where first the first mode which has planar movement along *x*-direction has a frequency of 3.47 kHz and this is the required mode since the proof mass is supposed to move in this direction. This second mode has out of plane motion i.e., along *z*-direction with a frequency of 5.30 kHz.

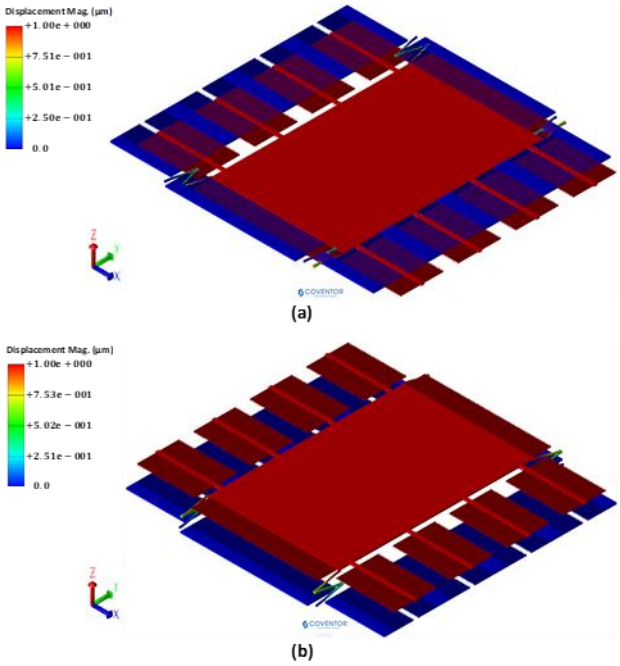

Figure 5.3: Eigen mode shapes for single axis accelerometer; (a) 1st mode along *x*-axis (3.47 kHz); (b) 2nd mode along *z*-axis (5.30 kHz).

5.3.2 Frequency Response Analysis

To determine the forced frequency response of the design at different input acceleration signals, harmonic analysis is performed while applying an input acceleration in steps of 10 g. Figure 5.4 shows curves obtained for different acceleration inputs i.e., from 10 g to 50 g and from the continuity of these curves it can be concluded that displacement of the proof mass has direct relationship with the magnitude of input acceleration. Similarly, the curves show a linear behaviour

in the region of starting frequency and is this is the desired operating region since linear operation is required.

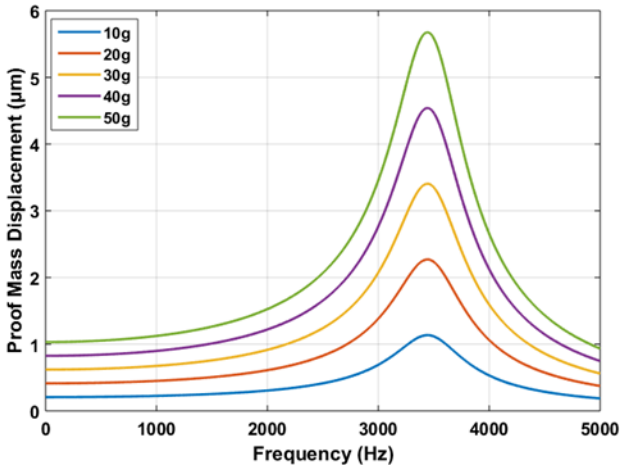

Figure 5.4: Harmonic response for MEMS accelerometer obtained at different acceleration inputs (10 g – 50 g).

5.3.3 Estimation of Pull-in Voltage

As discussed for the design presented before, the pull-in voltage is an important performance parameter which needs to be estimated to obtain the threshold voltage that can be applied for the working of the design. The mathematical equation to estimate pull-in voltage is the same as represented by Eq. (2.11).

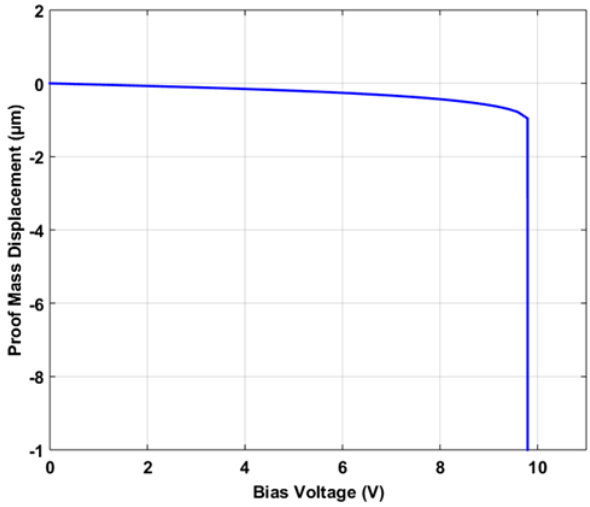

Figure 5.5: Pull-in voltage graph for the proposed design.

For this design, analysis for pull-in voltage is also done while giving varying voltage over a range of 0 to 10 V as shown by Fig. 5.5 and from the graph it can be concluded that pull-in phenomenon will occur if biasing voltage greater than or equal to 9.8 V is applied. So safe operating region for the design to work is below this pull-in value of 9.8 V.

5.3.4 Transient Study

To analyze the performance of the system when it moves from one steady state to another, transient analysis study is done the system of proposed design. As illustrated in Fig. 5.6(a), a input signal of magnitude equal to maximum allowable acceleration i.e., 5-0 g is applied dynamically at 100 Hz oscillating frequency. At start, before the signal the proof mass is stationary and initial delay of 5 ms is set to give the system sufficient time to reach steady state. From Fig. 5.6(b), it can be seen that before reaching to a new steady state, the proof mass oscillates and signal fall and rise time duration is 0.7 ms and on time is equal to 6 ms. The motional amplitude of the proof mass is 1.04 μm for this acceleration and hence the mechanical sensitivity is 0.021 μm/g.

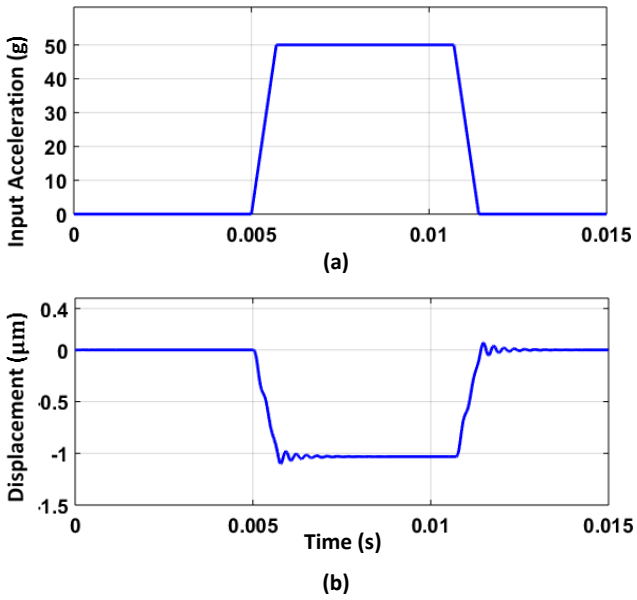

Figure 5.6: Obtained results of the transient study done on accelerometer using MATLAB and MEMS+.

5.3.5 Simulation for Capacitance Change

The main analysis of this study is to determine the capacitance change output when subjected to an input acceleration signal. Hence Multiphysics is developed with the integration of CoventorWare MEMS+ and MATLAB. Figure 5.7 illustrates the curve for capacitance change from −50 g to +50 g which reveals that the performance of the design in terms of capacitance output is almost linear with 4 pF as the maximum change in capacitance for ±50 g. Moreover, the value of rest capacitance is obtained as 10.26 pF and a capacitance sensitivity of 80.1 fF/g is estimated.

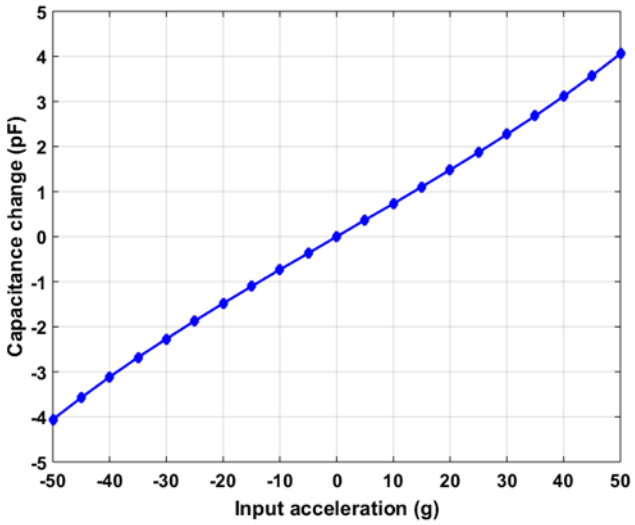

Figure 5.7: Capacitance change output against input acceleration for a range of −50 g to +50 g.

5.3.6 Discussion

Some of the other performance parameters for MEMS accelerometers include bandwidth, resolution, voltage sensitivity and quality factor. From results of the harmonic analysis shown in Fig. 5.4, the response is linear for a frequency range of DC-300 Hz, so this range can be considered as working bandwidth of the proposed design. The quality factor of the proof mass based on Eq. (2.14) is evaluated as 8.7. The resolution of the design depends on the capacitance sensitivity and the minimum detectable capability of the interfaced circuit. For our case, these values are 80.1 fF/g and 4 aF respectively and based on these values to the minimum motion of the proof mass that can be sensed can be against input acceleration as low as 2 mg.

5.3.7 Comparison with Literature

Table presents the comparison of the performance parameters of the proposed design with the ones reported previously it the literature [44, 66, 69]. For the proposed design for which the target application is inertial navigation, the performance parameters are comparable with others. The other designs are realized for different target applications such as seismic and low g. So natural frequency is set according to the requirements. If compared in terms of size, the designs an improvement in the value of the capacitance change as output. Similarly, the value of Brownian noise equivalent acceleration is also minimized.

Table 8: Comparison of the performance parameters with literature

Parameters	**This design**	**[44]**	**[66]**	**[69]**
Diemensions	4 mm × 3.9 mm	2 mm × 2 mm	5.7 mm × 2.3 mm	6 mm × 3.6 mm
Accelearatioon range	± 50g	± 5g	± 5g	± 2g
Resonant frequency	3472.13 Hz	4255 Hz	1430 Hz	503.803 Hz
Thickness (*t*)	25 µm	30 µm	30 µm	4 µm
Mechanical sensitivity	0.021 µm/g	0.014 µm/g	0.121 µm/g	1.075 µm/g
Capacitance sensitivity (c_s)	80.1 fF/g	35 fF/g	225 fF/g	66.7 fF/g
CNEA	49.93 µg/√Hz	114.3 µg/√Hz	17.78 µg/√Hz	3.166 µg/√Hz
BNEA	0.953 µg/√Hz	24 µg/√Hz	0.364 µg/√Hz	4.64 µg/√Hz
Bandwidth	DC-300 Hz	-	DC-100 Hz	DC-250 Hz
Quality factor	8.7	0.136	13	0.767

Chapter 6: Conclusions

This work reports a detailed working on the design of MEMS capacitive accelerometers considering the SOIMUMPs microfabrication process as target foundry for fabrication. A major part of this work deals with the design of a dual-axis MEMS capacitive accelerometer while presenting a smart, cost effective and time efficient design approach. This approach includes the optimization of dual-axis accelerometer using linked design and analysis of computer experiments and desirability function technique while using gradient descent algorithm.

The output parameters considered in the optimization include proof mass displacement, resonant frequency, capacitance change, Brownian noise equivalent acceleration (BNEA) and pull-in voltage. The optimization of these output parameters is done while finding the optimal values for input factors i.e., comb overlap length, width and lengths of mechanical spring beams, frequency ratio, temperature, input acceleration and pressure. At the beginning, a design matrix is made using Latin hypercube sampling technique of space filling design for computer experiments, then simulations based experiments are performed for each run as dictated by the design matrix and values of output responses are noted. Then meta-models are obtained by applying Gaussian process regression model using JMP statistical software to check the dependency of important input factors on each output parameter. Finally, to get the optimal values, an objective is defined which is later optimized using desirability function-based approach. The optimization method reveals the optimal values of 153.6 μm for overlap length between combs, 403.6 μm and 500 μm for the two lengths of spring beams, 6.2641 μm for the width of beams, 25 g for maximum input acceleration, 300 K for temperature, 760 Torr for pressure and 0.5 for frequency ratio. The predicted values of output parameters are 0.8061 $\mu g/\sqrt{Hz}$ for BNEA, 676.213 fF for change in capacitance, 3036.37 Hz for natural frequency, 6.7618 V for pull-in voltage and 0.9029 μm for mechanical displacement of proof mass with 0.688 as the value for total desirability. these predicted optimal values are later verified via FEM simulations and obtained values remained in the 95% confidence interval. Thus, the proposed methodology for optimization can be considered as efficient and robust and can be applied to other MEMS designs that have complex geometry and multiphysics involved.

After optimization, the works presents subsequent analysis done on the design which start with estimating mechanical and capacitance cross axis sensitivities which come out to be 0.0002 % and 0.028 %, respectively. Since the final output metric is voltage, so to estimate the voltage of for each value of acceleration, behavioral model of the design is integrated with Simulink tool of MATLAB in which a circuit is designed to mimic the operation of commercially available MS3110 IC and a curve showing the change in output voltage due the change in input acceleration is obtained. The total noise equivalent acceleration is found as 0.2 mg/$\sqrt{\text{Hz}}$ and the obtained working range for the design is $\pm$25 g.

The second part of the work presents the design of a capacitive MEMS accelerometer that focuses on the improvement in the design to enhance capacitance change and hence voltage sensitivity. This is achieved by designing rectangular shaped branch segments with the central proof mass to incorporate more combs. The performance is evaluated while estimating natural frequency, noises, pull-in voltage and change in capacitance and obtained values are 3.47 kHz for natural frequency, 9.8 V for pull-in, 80.1 fF/g for capacitance sensitivity and 0.953 μg/√Hz for BNEA.

References

[1] Gad-el-Hak, Mohamed, ed. *MEMS: introduction and fundamentals*. CRC press, 2005.

[2] Grayson, A. C. R., Shawgo, R. S., Johnson, A. M., Flynn, N. T., Li, Y., Cima, M. J., and Langer, R. (2004). A BioMEMS review: MEMS technology for physiologically integrated devices. *Proceedings of the IEEE*, *92*(1), 6-21.

[3] Holthoff, E. L., Heaps, D. A., and Pellegrino, P. M. (2010). Development of a MEMS-scale photoacoustic chemical sensor using a quantum cascade laser. *IEEE Sensors Journal*, *10*(3), 572-577.

[4] Beeby, S., Ensel, G., White, N. M., and Kraft, M. (2004). *MEMS mechanical sensors*. Artech House.

[5] Feynman, R. P. (1992). There's plenty of room at the bottom [data storage]. *Journal of microelectromechanical systems*, *1*(1), 60-66.

[6] Ghazali, F. A. M., Hasan, M. N., Rehman, T., Nafea, M., Ali, M. S. M., and Takahata, K. (2020). MEMS actuators for biomedical applications: a review. *Journal of Micromechanics and Microengineering*, *30*(7), 073001.

[7] Nisar, A., Afzulpurkar, N., Mahaisavariya, B., and Tuantranont, A. (2008). MEMS-based micropumps in drug delivery and biomedical applications. *Sensors and Actuators B: Chemical*, *130*(2), 917-942.

[8] Khoshnoud, F., and de Silva, C. W. (2012). Recent advances in MEMS sensor technology–biomedical applications. *IEEE Instrumentation & Measurement Magazine*, *15*(1), 8-14.

[9] Bogue, R. (2013). Recent developments in MEMS sensors: A review of applications, markets and technologies. *Sensor Review*.

[10] Schadow, K. (2004, November). MEMS military Applications-RTO task group summary. In *CANEUS 2004 Conference on Micro-Nano-Technologies* (p. 6749).

[11] Bhatt, G., Manoharan, K., Chauhan, P. S., and Bhattacharya, S. (2019). MEMS sensors for automotive applications: a review. *Sensors for Automotive and Aerospace Applications*, 223-239.

[12] Nihtianov, S., and Luque, A. (Eds.). (2018). *Smart sensors and MEMS: Intelligent sensing devices and microsystems for industrial applications*. Woodhead Publishing.

[13] Ayazi, F. (2011, June). Multi-DOF inertial MEMS: From gaming to dead reckoning. In *2011 16th International Solid-State Sensors, Actuators and Microsystems Conference* (pp. 2805-2808). IEEE.

[14] Yazdi, N., Ayazi, F., and Najafi, K. (1998). Micromachined inertial sensors. *Proceedings of the IEEE*, *86*(8), 1640-1659.

[15] Finkbeiner, S. (2013, September). MEMS for automotive and consumer electronics. In *2013 Proceedings of the ESSCIRC (ESSCIRC)* (pp. 9-14). IEEE.

[16] Guan, L., Xu, X., Gao, Y., Liu, F., Rong, H., Wang, M., and Noureldin, A. (2018). Micro-Inertial-Aided High-Precision Positioning Method for Small-Diameter PIG Navigation. In *Advances in Human and Machine Navigation Systems*. IntechOpen.

[17] Mohammed, Z., Elfadel, I. A. M., and Rasras, M. (2018). Monolithic multi degree of freedom (MDoF) capacitive MEMS accelerometers. *Micromachines*, *9*(11), 602.
[18] Luczak, S. (2014). Effects of misalignments of MEMS accelerometers in tilt measurements. In *Mechatronics 2013* (pp. 393-400). Springer, Cham.
[19] Rödjegård, H., Johansson, C., Enoksson, P., and Andersson, G. (2005). A monolithic three-axis SOI-accelerometer with uniform sensitivity. *Sensors and Actuators A: Physical*, *123*, 50-53.
[20] Tez, S., Aykutlu, U., Torunbalci, M. M., and Akin, T. (2015). A bulk-micromachined three-axis capacitive MEMS accelerometer on a single die. *Journal of Microelectromechanical Systems*, *24*(5), 1264-1274.
[21] Merdassi, A., Kezzo, M. N., Xereas, G., and Chodavarapu, V. P. (2015). Wafer level vacuum encapsulated tri-axial accelerometer with low cross-axis sensitivity in a commercial MEMS Process. *Sensors and Actuators A: Physical*, *236*, 25-37.
[22] Comi, C., Corigliano, A., Langfelder, G., Longoni, A., Tocchio, A., and Simoni, B. (2010). A resonant microaccelerometer with high sensitivity operating in an oscillating circuit. *Journal of microelectromechanical systems*, *19*(5), 1140-1152.
[23] Yang, J., Zhang, M., Si, C., Han, G., Ning, J., Yang, F., and Wang, X. (2019). A T-shape aluminum nitride thin-film piezoelectric MEMS resonant accelerometer. *Journal of Microelectromechanical Systems*, *28*(5), 776-781.
[24] Ding, H., Wang, W., Ju, B. F., and Xie, J. (2017). A MEMS resonant accelerometer with sensitivity enhancement and adjustment mechanisms. *Journal of Micromechanics and Microengineering*, *27*(11), 115010.
[25] Wang, S., Wei, X., Zhao, Y., Jiang, Z., and Shen, Y. (2018). A MEMS resonant accelerometer for low-frequency vibration detection. *Sensors and Actuators A: Physical*, *283*, 151-158.
[26] Zhao, C., Liu, H., Song, P., & Hu, F. (2020). Micro-electrometer Based on Mode-Localization Effect. In *Micro and Nano Machined Electrometers* (pp. 43-81). Springer, Singapore.
[27] Zhang, H., Li, B., Yuan, W., Kraft, M., and Chang, H. (2016). An acceleration sensing method based on the mode localization of weakly coupled resonators. *Journal of microelectromechanical systems*, *25*(2), 286-296.
[28] Peng, B., Hu, K. M., Shao, L., Yan, H., Li, L., Wei, X., and Zhang, W. M. (2019). A sensitivity tunable accelerometer based on series-parallel electromechanically coupled resonators using mode localization. *Journal of Microelectromechanical Systems*, *29*(1), 3-13.
[29] Pandit, M., Zhao, C., Sobreviela, G., Zou, X., and Seshia, A. (2019). A high resolution differential mode-localized MEMS accelerometer. *Journal of Microelectromechanical Systems*, *28*(5), 782-789.
[30] Zhao, C., Wood, G. S., Xie, J., Chang, H., Pu, S. H., and Kraft, M. (2015). A three degree-of-freedom weakly coupled resonator sensor with enhanced stiffness sensitivity. *Journal of Microelectromechanical Systems*, *25*(1), 38-51.
[31] Monajemi, P., and Ayazi, F. (2006). Design optimization and implementation of a microgravity capacitive HARPSS accelerometer. *IEEE Sensors journal*, *6*(1), 39-46.

[32] Roy, A. L., and Bhattacharyya, T. K. (2015). Design, fabrication and characterization of high performance SOI MEMS piezoresistive accelerometers. *Microsystem Technologies*, *21*(1), 55-63.

[33] Zandi, K., Bélanger, J. A., and Peter, Y. A. (2012). Design and demonstration of an in-plane silicon-on-insulator optical MEMS Fabry–Pérot-based accelerometer integrated with channel waveguides. *Journal of Microelectromechanical systems*, *21*(6), 1464-1470.

[34] Mukherjee, R., Guha, P. K., and Mandal, P. (2016). Sensitivity improvement using optimized heater design for dual axis thermal accelerometers. *Microsystem Technologies*, *22*(10), 2475-2485.

[35] Wang, Y. H., Song, P., Li, X., Ru, C., Ferrari, G., Balasubramanian, P., and Liu, X. (2018). A paper-based piezoelectric accelerometer. *Micromachines*, *9*(1), 19.

[36] Antunes, P. F. C., Marques, C. A., Varum, H., and Andre, P. S. (2012). Biaxial optical accelerometer and high-angle inclinometer with temperature and cross-axis insensitivity. *IEEE Sensors Journal*, *12*(7), 2399-2406.

[37] Gonenli, I. E., Celik-Butler, Z., and Butler, D. P. (2011). Surface micromachined MEMS accelerometers on flexible polyimide substrate. *IEEE Sensors Journal*, *11*(10), 2318-2326.

[38] Tsai, M. H., Liu, Y. C., and Fang, W. (2012). A three-axis CMOS-MEMS accelerometer structure with vertically integrated fully differential sensing electrodes. *Journal of microelectromechanical systems*, *21*(6), 1329-1337.

[39] Serrano, D. E., Jeong, Y., Keesara, V., Sung, W. K., and Ayazi, F. (2014, January). Single proof-mass tri-axial pendulum accelerometers operating in vacuum. In *2014 IEEE 27th International Conference on Micro Electro Mechanical Systems (MEMS)* (pp. 28-31). IEEE.

[40] Köse, T., Terzioğlu, Y., Azgın, K., and Akın, T. (2015, March). A single mass two-axis capacitive MEMS accelerometer with force rebalance. In *2015 IEEE International Symposium on Inertial Sensors and Systems (ISISS) Proceedings* (pp. 1-4). IEEE.

[41] Tsai, M. H., Liu, Y. C., Liang, K. C., and Fang, W. (2015). Monolithic CMOS—MEMS pure oxide tri-axis accelerometers for temperature stabilization and performance enhancement. *Journal of Microelectromechanical Systems*, *24*(6), 1916-1927.

[42] Yamane, D., Matsushima, T., Konishi, T., Toshiyoshi, H., Masu, K., and Machida, K. (2016). A dual-axis MEMS capacitive inertial sensor with high-density proof mass. *Microsystem Technologies*, *22*(3), 459-464.

[43] Aydemir, A., Terzioglu, Y., and Akin, T. (2016). A new design and a fabrication approach to realize a high performance three axes capacitive MEMS accelerometer. *Sensors and Actuators A: Physical*, *244*, 324-333.

[44] Mohammed, Z., Dushaq, G., Chatterjee, A., and Rasras, M. (2018). An optimization technique for performance improvement of gap-changeable MEMS accelerometers. *Mechatronics*, *54*, 203-216.

[45] Mukherjee, T., Iyer, S., and Feeder, G. K. (1998). Optimization-based synthesis of microresonators. *Sensors and Actuators A: Physical*, *70*(1-2), 118-127.

[46] Benmessaoud, M., and Nasreddine, M. M. (2013). Optimization of MEMS capacitive accelerometer. *Microsystem technologies*, *19*(5), 713-720.

[47] Liu, Y., Yang, H. Y., and Wang, G. C. (2012). Genetic algorithm based multidisciplinary design optimization of MEMS accelerometer. In *Applied Mechanics and Materials* (Vol. 101, pp. 530-533). Trans Tech Publications Ltd.

[48] Giannini, D., Braghin, F., and Aage, N. (2020). Topology optimization of 2D in-plane single mass MEMS gyroscopes. *Structural and Multidisciplinary Optimization*, *62*(4), 2069-2089.

[49] Keshavarzi, M., and Hasani, J. Y. (2019). Design and optimization of fully differential capacitive MEMS accelerometer based on surface micromachining. *Microsystem Technologies*, *25*(4), 1369-1377.

[50] Ramakrishnan, J., Gaurav, P. R., Chandar, N. S., and Sudharsan, N. M. (2021). Structural design, analysis and DOE of MEMS-based capacitive accelerometer for automotive airbag application. *Microsystem Technologies*, *27*(3), 763-777.

[51] Li, R., Mohammed, Z., Rasras, M., Elfadel, I. A. M., and Choi, D. (2021). Design, modelling and characterization of comb drive MEMS gap-changeable differential capacitive accelerometer. *Measurement*, *169*, 108377.

[52] Beg, S., Swain, S., Rahman, M., Hasnain, M. S., and Imam, S. S. (2019). Application of design of experiments (DoE) in pharmaceutical product and process optimization. In *Pharmaceutical quality by design* (pp. 43-64). Academic Press.

[53] Hoshmand, R. (2006). *Design of Experiments for Agriculture and the Natural Sciences Second Edition*. CRC Press.

[54] Malakizadi, A., Cedergren, S., Sadik, I., and Nyborg, L. (2016). Inverse identification of flow stress in metal cutting process using Response Surface Methodology. *Simulation Modelling Practice and Theory*, *60*, 40-53.

[55] Saleem, M. M., and Somá, A. (2015). Design of experiments based factorial design and response surface methodology for MEMS optimization. *Microsystem Technologies*, *21*(1), 263-276.

[56] Saleem, M. M., Farooq, U., Izhar, U., and Khan, U. S. (2017). Multi-response optimization of electrothermal micromirror using desirability function-based response surface methodology. *Micromachines*, *8*(4), 107.

[57] Younis, S., Saleem, M. M., Zubair, M., and Zaidi, S. M. T. (2018). Multiphysics design optimization of RF-MEMS switch using response surface methodology. *Microelectronics Journal*, *71*, 47-60.

[58] Wang, M., Lv, W., Yang, F., Yan, C., Cai, W., Zhou, D., and Zeng, X. (2017). Efficient yield optimization for analog and sram circuits via gaussian process regression and adaptive yield estimation. *IEEE Transactions on Computer-Aided Design of Integrated Circuits and Systems*, *37*(10), 1929-1942.

[59] Sanabria-Borbón, A. C., Soto-Aguilar, S., Estrada-López, J. J., Allaire, D., and Sánchez-Sinencio, E. (2020). Gaussian-Process-Based Surrogate for Optimization-Aided and Process-Variations-Aware Analog Circuit Design. *Electronics*, *9*(4), 685.

[60] Akin, A., and Kahveci, H. S. (2019). An optimization study for rotorcraft avionics bay cooling. *Aerospace Science and Technology*, *90*, 1-11.

[61] Fan, X., Wang, P., and Hao, F. (2019). Reliability-based design optimization of crane bridges using Kriging-based surrogate models. *Structural and Multidisciplinary Optimization*, *59*(3), 993-1005.
[62] Sacks, J., Welch, W. J., Mitchell, T. J., and Wynn, H. P. (1989). Design and analysis of computer experiments. *Statistical science*, 409-423.
[63] Mo, Y., Zhou, H., Xie, G., and Tang, B. (2018). Investigation of air damping effect in two kinds of capacitive MEMS accelerometers. *Microsystem Technologies*, *24*(4), 2017-2023.
[64] Cowen, A., Hames, G., Monk, D., Wilcenski, S., and Hardy, B. (2011). SOIMUMPs design handbook. *MEMSCAP Inc*, 2002-2011.
[65] Dwivedi, A., and Khanna, G. (2019). Numerical simulation and modelling of a novel MEMS capacitive accelerometer based microphone for fully implantable hearing aid. *Microsystem Technologies*, *25*(2), 399-411.
[66] Mukhiya, R., Agarwal, P., Badjatya, S., Garg, M., Gaikwad, P., Sinha, S., Singh, A.K., and Gopal, R. (2019). Design, modelling and system level simulations of DRIE-based MEMS differential capacitive accelerometer. *Microsystem Technologies*, *25*(9), 3521-3532.
[67] Singiresu, S. R. (1995). *Mechanical vibrations*. Boston, MA: Addison Wesley.
[68] Wai-Chi, W., Azid, A. A., and Majlis, B. Y. (2010). Formulation of constant and effective mass for a folded beam. *Archives of Mechanics*, *62*(5), 405-418.
[69] Kavitha, S., Daniel, R. J., and Sumangala, K. (2016). Design and analysis of MEMS comb drive capacitive accelerometer for SHM and seismic applications. *Measurement*, *93*, 327-339.
[70] Zhang, H., Wei, X., Ding, Y., Jiang, Z., and Ren, J. (2019). A low noise capacitive MEMS accelerometer with anti-spring structure. *Sensors and Actuators A: Physical*, *296*, 79-86.
[71] Jeong, Y., Serrano, D. E., and Ayazi, F. (2017). Low-pressure wafer-level-packaged capacitive accelerometers with high dynamic range and wide bandwidth using nano-gap sloped electrode design. *Journal of Microelectromechanical Systems*, *26*(6), 1335-1344.
[72] Dai, G., Li, M., He, X., Du, L., Shao, B., and Su, W. (2011). Thermal drift analysis using a multiphysics model of bulk silicon MEMS capacitive accelerometer. *Sensors and Actuators A: Physical*, *172*(2), 369-378.
[73] Dong, X., Huang, Q., Xu, W., Tang, B., Yang, S., Zhu, J., and En, Y. (2019). Research on temperature characteristic of parasitic capacitance in MEMS capacitive accelerometer. *Sensors and Actuators A: Physical*, *285*, 581-587.
[74] Jeong, Y., Serrano, D. E., Keesara, V., Sung, W. K., and Ayazi, F. (2013, January). Wafer-level vacuum-packaged triaxial accelerometer with nano airgaps. In *2013 IEEE 26th International Conference on Micro Electro Mechanical Systems (MEMS)* (pp. 33-36). IEEE.
[75] Choa, S. H. (2005). Reliability of MEMS packaging: vacuum maintenance and packaging induced stress. *Microsystem technologies*, *11*(11), 1187-1196.
[76] Edalatfar, F., Yaghootkar, B., Qureshi, A. Q. A., Azimi, S., and Bahreyni, B. (2016, October). Design, fabrication and characterization of a high performance MEMS accelerometer. In *2016 IEEE SENSORS* (pp. 1-3). IEEE.

[77] Serrano, D. E., Jeong, Y., Keesara, V., Sung, W. K., and Ayazi, F. (2014, January). Single proof-mass tri-axial pendulum accelerometers operating in vacuum. In *2014 IEEE 27th International Conference on Micro Electro Mechanical Systems (MEMS)* (pp. 28-31). IEEE.

[78] Somà, A., Saleem, M. M., and De Pasquale, G. (2016). Effect of creep in RF MEMS static and dynamic behavior. *Microsystem Technologies*, *22*(5), 1067-1078.

[79] Gabrielson, T. B. (1993). Mechanical-thermal noise in micromachined acoustic and vibration sensors. *IEEE transactions on Electron Devices*, *40*(5), 903-909.

[80] Amini, B. V., Abdolvand, R., and Ayazi, F. (2005, June). Sub-micro-gravity capacitive SOI microaccelerometers. In *The 13th International Conference on Solid-State Sensors, Actuators and Microsystems, 2005. Digest of Technical Papers. TRANSDUCERS'05.* (Vol. 1, pp. 515-518). IEEE.

[81] Syed, W. U., Brimmo, A., Waheed, O., Bojesomo, A., Ali, M. H., Ocak, I., Chengliang, S., Chatterjee, A., and Elfadel, I. A. M. (2017). Numerical modeling and validation of squeezed-film damping in vacuum-packaged industrial MEMS. *Journal of Micromechanics and Microengineering*, *27*(7), 075016.

[82] Mol, L., Rocha, L. A., Cretu, E., and Wolffenbuttel, R. F. (2009). Squeezed film damping measurements on a parallel-plate MEMS in the free molecule regime. *Journal of micromechanics and microengineering*, *19*(7), 074021.

[83] Veijola, T., and Raback, P. (2007). Methods for solving gas damping problems in perforated microstructures using a 2D finite-element solver. *Sensors*, *7*(7), 1069-1090.

[84] Morris, C. J., and Forster, F. K. (2004). Oscillatory flow in microchannels. *Experiments in Fluids*, *36*(6), 928-937.

[85] Gonenli, I. E., Celik-Butler, Z., and Butler, D. P. (2011). Surface micromachined MEMS accelerometers on flexible polyimide substrate. *IEEE Sensors Journal*, *11*(10), 2318-2326.

[86] Snelson, E. L. (2007). *Flexible and efficient Gaussian process models for machine learning* (Doctoral dissertation, UCL (University College London)).

[87] Jones, B., and Johnson, R. T. (2009). Design and analysis for the Gaussian process model. *Quality and Reliability Engineering International*, *25*(5), 515-524.

[88] Montgomery, D. C. (2013). Montgomery Design and Analysis of Experiments Eighth Edition. Arizona State University. *Copyright*, *2009*(2005), 2001.

[89] Rasmussen, C. E. (2003, February). Gaussian processes in machine learning. In *Summer school on machine learning* (pp. 63-71). Springer, Berlin, Heidelberg.

[90] Kang, F., Han, S., Salgado, R., and Li, J. (2015). System probabilistic stability analysis of soil slopes using Gaussian process regression with Latin hypercube sampling. *Computers and Geotechnics*, *63*, 13-25.

[91] Viana, F. A. (2016). A tutorial on Latin hypercube design of experiments. *Quality and reliability engineering international*, *32*(5), 1975-1985.

[92] McKaya, M. D., Beckmana, R. J., and Conoverb, W. J. (1979). Comparison of three methods for selecting values of input variables in the analysis of output from a computer code. *Technometrics*, *21*(2), 239-245.

[93] Ko, Y. H., Kim, K. J., and Jun, C. H. (2005). A new loss function-based method for multiresponse optimization. *Journal of Quality Technology*, *37*(1), 50-59.
[94] Khuri, A. I., and Conlon, M. (1981). Simultaneous optimization of multiple responses represented by polynomial regression functions. *Technometrics*, *23*(4), 363-375.
[95] Del Castillo, E., Montgomery, D. C., and McCarville, D. R. (1996). Modified desirability functions for multiple response optimization. *Journal of quality technology*, *28*(3), 337-345.
[96] Harrington, E. C. (1965). The desirability function. *Industrial quality control*, *21*(10), 494-498.
[97] Derringer, G., and Suich, R. (1980). Simultaneous optimization of several response variables. *Journal of quality technology*, *12*(4), 214-219.
[98] Riaz, K., Bazaz, S. A., Saleem, M. M., and Shakoor, R. I. (2011). Design, damping estimation and experimental characterization of decoupled 3-DoF robust MEMS gyroscope. *Sensors and Actuators A: Physical*, *172*(2), 523-532.
[99] Cauchi, M., Grech, I., Mallia, B., Mollicone, P., and Sammut, N. (2018, September). The effects of structure thickness, air gap thickness and silicon type on the performance of a horizontal electrothermal MEMS microgripper. In *Actuators* (Vol. 7, No. 3, p. 38). Multidisciplinary Digital Publishing Institute.
[100] MS3110 Datasheet, Irvine Sensors Corporation, Costa Mesa, CA.
[101] Chen, W., Ding, J., Liu, X., and Wang, C. (2007, January). Design and system-level simulation of a capacitive dual axis accelerometer. In *2007 2nd IEEE International Conference on Nano/Micro Engineered and Molecular Systems* (pp. 614-617). IEEE.

Completion Certificate

It is certified that the contents of thesis document titled "***Design of a Dual-Axis Capacitive MEMS Accelerometer for Low Cross-Axis Sensitivity and Low Noise using SOIMUMPs Process***" submitted by NS Shayaan Saghir, Registration No. 00000274053 have been found satisfactory in all respects as per the requirements of Main Office, NUST (Exam branch).

Supervisor: _____

Dr. Muhammad Mubasher Saleem

Date: ____ April, 2021